Superhydrophobic Surfaces based on TiO_2 Nanostructures, Synthesis and Applications

By

Weidi Hua

A thesis submitted in partial of fulfillment of the requirements of the degree of

Master of Science

In

Solid State Electronics

Department of Electrical and Computer Engineering

University of Alberta

Abstract

Multiple superhydrophobic surfaces are fabricated based on TiO_2 nanostructures, which have a wide swathe of potential applications in industry, where hydrophobic surfaces are in great demand. Three different fabrication methods − electrochemical anodization, hydrothermal formation, and spray coating, are all used to generate different nanostructures in order to adapt to different surfaces and environments; each is also a simple and low cost method of synthesis. These fabricated surfaces are proven to be resistant to harsh conditions such as ultrasound vibration, water fouling, as well as abrasion, and experiments are performed to demonstrate these properties. Among them, the surface that is produced by hydrothermal synthesis is optically transparent, which is desirable in applications such as stain-free car windshields or superhydrophobic spectroscopy windows. Finally, an electrowetting on dielectric (EWOD) device is also fabricated on the hydrophobic surface, as it aligns well with the construction of a typical EWOD device, using TiO_2 instead of a dielectric polymer. Actuation of a liquid is observed on these devices, as seen in the change of contact angle.

Preface

A portion of the research conducted for this thesis is part of a collaboration, between the University of Alberta and Technische Universität München (TUM) through the ATUMS initiative. The coating mentioned in Chapter 6 is fabricated by Weidi Hua using the TUM facility. SEM imaging in section 6.3.1, ASTM D968-17 testing and Dektak 3D depth mapping in section 6.3.3 were performed by Mr. Marco Bobinger from TUM.

The ultrasound resistance of titania nanotube array grown in aqueous electrolyte mentioned in Chapter 3 was studied in a collaboration between Weidi Hua, Dr. Partha Roy and Lintong Bu. The FTIR mentioned in Section 3.3 was performed by Dr. Partha Roy. The results in Chpater 3 are part of a manuscript titled "Resistance of Superhydrophobic Surface-Functionalized TiO2 Nanotubes to Corrosion and Intense Cavitation", which has been submitted for publication as a journal article, and is in the final stages of peer review. The results in Chapter 4 have been compiled into a manuscript titled "Threshold Hydrophobicity for Inhibition of Salt Scale Formation on SAM-Modified Titania Nanotube Arrays", and submitted for publication as a journal article. The superhydrophobic transparent titania nanowire surface mentioned in Chapter 5 was fabricated by Ujwal Thakur. The SEM and UV-VIS data mentioned in Section 5.3 were obtained by Ujwal Thakur. The superhydrophobic transparent titania nanowire surface and the superhydrophobic titania nanotube array were fabricated by Arezoo Hosseini.

Acknowledgements

First, I would like to thank Dr. Karthik Shankar, who is not only a great supervisor, but also a compassionate person that cares about others. Just by simply discussing with him, numerous great research ideas emerged, which then turned into great research projects during the short two years. A truly inspiring mentor I must say. I am improved in many ways during the time I spent in the Shankar Lab, and I could not find a matching experience to compare with it.

I would also like to thank my colleagues, both in Canada and Germany. I felt lucky that I can be part of the ATUMS international graduate study program, a great initiative run by a group of great people. The list of persons to thank are, from U of A: Dr. Jon Veinot for running ATUMs, Leah Veinot for taking care of every ATUMS event and every ATUMS student. Additionally from the Shankar Lab: Dr. Arash Mohammadpour, Dr. Samira Farsinezhad, Dr. Piyush Kar, Dr. Partha Roy, Benjamin Wiltshire, Ryan Kisslinger, Arezoo Hosseini, Abdelrahman Askar, Mourad Benlamri, Lintong Bu, Yun Zhang, Ujwal Thakur, Najia Mahdi, Advaita Bhatnagar; and from Germany side: Dr. Markus Becherer, Marco Bobinger, Alina Lyuleeva, Andreas Albrecht, Michael Haider, Marius Loch, Josef Mock, Kamyar Baghvand, Jacopo Bonaccini Calia, Dr. Saba Suladze, and so many more.

I would also thank my parents, for supporting me along the way, for their understanding and great patience; my grandfather, for taking care of me since I was born; as well as Miss Angelina Zhu, meeting you is the luckiest thing that happened in my life. Thank you all and because of all your love and support I could keep continuing to improve myself and moving forward.

Table of Contents

Abstract ii
Preface iii
Acknowledgements iv
Table of Contents v
List of Figures vii
List of Abbreviations x
Chapter 1. Introduction 1
1.1 The Current Physics Model of Wetting 1
1.1.1 The discovery of superhydrophobicity in nature 1
1.1.2 Young's Equation 1
1.1.3 Wenzel and Cassie-Baxter state 3
1.2 Titanium Oxide Nanostructure-Based Superhydrophobic Surfaces 4
1.2.1 Overview of Recent Research Trends on Hydrophobic Surfaces 4
1.2.2 Overview of TiO_2 as a Material 5
1.2.3 Introduction to Electrochemically Formed Titanium Oxide Nanostructures 5
1.3 Introduction to Self-Assembled Monolayers (SAMs) and Their Role in Surface Modification Processes 10
1.4 Introduction to Superhydrophobic Coating Based On Nanoparticles 12
1.5 Introduction of Electrowetting-on-Dielectric (EWOD) 13
Chapter 2. TNAs Based Superhydrophobic Surface and Relation between Length of Nanotubes and Hydrophobicity 15
2.1 Introduction to TNA-Based Superhydrophobic Surface 15
2.2 Preparation of Superhydrophobic TNAs 16
2.2.1 Materials Used 16
2.2.2 Preparation Procedure 16
2.3 Results and Discussion 17
2.3.1 Contact Angle Measurements 17
2.3.2 The Sticking Surface versus Non-Sticking Surface 20
2.4 Conclusion 22
Chapter 3. TNA-based Ultrasound Resistant Superhydrophobic Surface 23
3.1 Introduction to Ultrasound Resistant TNAs 23

3.2 Preparation of Superhydrophobic TiO_2 nanotubes 23
3.2.1 Preparation of Aqueous Based TNAs 23
3.2.2 Functionalization 24
3.3 Results and Discussion 24
3.4 Conclusion 30
Chapter 4. TNA-Based Anti-Fouling Superhydrophobic Surface 31
4.1 Introduction of TNA-Based Anti-Fouling Superhydrophobic Surface 31
4.2 The Anti-Fouling Test 32
4.3 Results and Discussion 33
4.4 Conclusion 35
Chapter 5. Transparent TiO_2 Nanowire Arrays (TNWs) Superhydrophobic Surface 36
5.1 Introduction to TNWs Superhydrophobic Surface 36
5.2 Preparation Procedure of Transparent Superhydrophobic TNWs 37
5.3 Results and Discussion 38
5.4 Conclusion 40
Chapter 6. Superhydrophobic Coating Based On TiO_2 Nanoparticles (NPs) and Polydimethylsiloxane (PDMS) 42
6.1 Introduction to coating based on TiO_2 NPs and PDMS 42
6.2 Preparation Procedure 42
6.2.1 Materials 42
6.2.2 Suspension Preparation and coating procedure 43
6.3 Results and Discussion 43
6.3.1 Morphology of the coating 43
6.3.2 Study of Fabrication Optimization 45
6.3.3 Robustness of the sprayed film 45
6.4 Conclusion 47
Chapter 7. Electrowetting on Functionalized Nanowire & Nanotube Surfaces 48
7.1 Introduction of EWOD on Superhydrophobic TNAs and TNWs 48
7.2 Preparation of the EWOD Setup of Superhydrophobic TNAs and TNWs 49
7.3 Results and Discussion 50
7.4 Conclusion 51
Chapter 8. Summary 52
Biliography 54

List of Figures

Figure	Description	Page No.
Figure 1	(a) The contact angle derivation. (b) Left, Wenzel type wetting model, right, Cassie-Baxter type wetting model	3
Figure 2	Figure 1. a) Drawing of an anodization setup. b) Typical current vs time plot for an anodization process. Solid and dashed lines represents the presence and absence of F^- ions, respectively. A compact oxide layer is obtained when there is no F^- ions as opposed to a honeycomb/tube-array structure is obtained with F^- ions. The honeycomb/tube-array structure has a three-stage formation process. Inset is a current potential plot, where the dot lines, solid lines, and the dashed line represents a high F^- content electrolyte, a medium F^- content electrolyte, and a low F^- content, respectively. c) d) are reaction mechanism for field assist ion transport during the anodizing, where in c) the electrolyte is F^- free while d) has F^- ions. (Modified with permission from Angew. Chem. Int. Ed. 2011, 50, 2904 – 2939. Copyrights, 2001 Wiley and Sons).	7
Figure 3	Figure 2: Left Part, SEM micrographs of nanowires prepared by Hosono et al. Right Part, the TNWs prepared by Liu et al. Adapted with permission from Hosono, E.; Fujihara, S.; Kakiuchi, K.; Imai, H. J. Am. Chem. Soc. 2004, 126, 7790–7791.Copyright 2004 American Chemical Society. (Left Part)(25) Adapted with permission from Bin L and Eray A. J. Am. Chem. Soc. 2009 *131* (11), 3985-3990. Copyright 2009 American Chemical Society. (Right Part) (29)	9
Figure 4	Immersing method formed SAMs. SAMs will formed on the surface due to spontaneous heat motion when immersed in a non-polar solution. Reprinted with permission from Chem. Rev. 1996, 96, 1533−1554. Copyright 1995 American Chemical Society (31)	11
Figure 5	The process of producing the nanoparticle-polymer blend based superhydrophobic coating (40). © 2010 National Institute for Materials Science	12
Figure 6	Figure 3: Left Part, schematic of changing of the water contact angle of a traditional electrowetting device without a bias, (b), with bias. Right Part Schematic of changing of the water contact angle on a EWOD. (a) Without a bias, (b) With a bias. The field drives the reduction in contact angle as shown in (b). Reprinted from, with the permission of AIP Publishing.[45]	14
Figure 7	(a) The relation between anodization time and contact angle after functionalization. (b) The relation between length of nanotubes and anodization time.	17

Figure 8	The TNA surface area calculation model derived by Farsinezhad et al. Reproduced from (48) with permission of The Royal Society of Chemistry.	18
Figure 9	(a) 30 min anodization, 5 µm TNAs (b) 1 hour anodization, 8 µm TNAs (c) 1.5 hours anodization, 12 µm TNAs (d) 2 hours anodization, 14 µm TNA. Inset: and the zoom-in view a random picked area, the yellow shaded areas indicate some of the "missing areas"- the gaps generated from the process of removing the top debris layer of the TNAs.	20
Figure 10	Process flow of TNA fabrication: (a)From top to bottom: The cleaned (Ultrasonicated in acetone, methanol, water, for 10 minutes each) Ti foil before anodization; the TNA grown on the Ti foil in water based electrolyte, ~16 hours growth time, molecular coating is applied to functionalize the surface (PFDPA or ODPA in methanol as the functionalization solution, sample immersed for 24 hours), (b) Example of contact angle measurement shows superhydrophobicity of the functionalized(with ODPA) surface.	25
Figure 11	FE-SEM image of the TNAs, the main picture shows the overlook and the edge of the TNA sample that formed on Ti foil, where the top right inset is a zoomed-in view of the TNAs and the bottom left inset is a zoomed-in view of the length of the nanotubes measured from their edge.	26
Figure 12	IR spectra: (a) C-H spectrum of functionalized TNAs before ultrasound (Black) and after ultrasound (Red),(b) C-H spectrum of TNAs recovered from ultrasonic treatment, (c) C-F stretching region of bare and PFDPA monolayer coated TNAs, respectively. All spectrums have been normalized.	28
Figure 13	Contact angle measurements of superhydrophobic surfaces at different stages: (a) a cleaned bare TNA surface, TNA surface functionalized by (b) ODPA and (c) PFDPA molecules, respectively, (d) ODPA and (e) PFDPA functionalized TNA surfaces after 60 minute of ultrasound, (f) PFDPA and (g) ODPA functionalized surface after 70 minutes of ultrasound, with superhydrophobicity lost; (h)ODPA and (9)PFDPA functionalized surface after being placed in ambient overnight.	29
Figure 14	Process flow of making the superhydrophobic TNAs (1-4) and the anti-fouling test (5-7).	32
Figure 15	(a) The sample of half functionalized TNAs surface in water, red circle shows air gap between surface and water. (b) After the liquid is evaporated, red circle shows functionalized surface, (c) with salt water, after the liquid evaporated, (d) after the test repeat for three times (e) Five times.	33
Figure 16	(a) photograph (left) and SEM image with EDX map scan marked (right) of the partially functionalized TNAs. (b) Maps of single elements. (c)List of the elements and weight percentage.	34
Figure 17	Schematic representation of the making of transparent superhydrophobic surfaces	38

Figure 18	The top view of the TNWs array. (b) The side view of the TNWs array, shows the random orientation of the TNWs. Inset: The contact angle of the transparent sample, showing a 157.18° contact angle.	39
Figure 19	The UV-Vis spectra of the PFDPA coated TiO2 nanowire array on FTO glass.	40
Figure 20	Image of (a) the suspension of TiO2-PDMS. (b) The triplex II air brush. (c) The contact angle of the obtained film, with a droplet of 10μL of DI water.	43
Figure 21	LM (a) and SEM (b), (c), (d) images showing the micro- and nano-structures of the coating. 2(a), Micro-sized features that looks like rocks, which scattered everywhere; these are actually agglomerations of TiO2 nanoparticles sealed in PDMS. 2(b), 2(c) and 2(d) shown a "zoomed-in" view from 5000 times magnification to 80,000 times. It can be clearly seen that the nano-sized features exist on the micro-sized features.	44
Figure 22	(a) and (b) LM image the before and after 5L of sand abraded coating.(c) and (d), the 3D depth map of before and after abraded coating. Insets: The photo graph for CA measurement for (a) and (b).	46
Figure 23	Photographs of TNWs (a) and TNAs (b) setup. (c) Scheme of the TNAs or TNWs EWOD setup.	49
Figure 24	Images of response of a droplet on superhydrophobic TNAs surface when applied constant bias as time ellipse.(a) Starting off,(b) 60s (c) 150s (d) 240s.	50
Figure 25	Two water droplets standing on the TNW superhydrophobic surface. The droplet at left has been subjected to a bias while the droplet on the right is not.	51

List of Abbreviations

Abbreviation	Description	First Use
WCA	Water Contact Angle	1
SEM	Scanning Electron Microscopy	1
CVD	Chemical Vapor Deposition	4
PVD	Physical Vapor Deposition	4
FDA	Food And Drug Administration	4
Tnas	Titanium Oxide Nanotube Arrays	5
ALD	Tomic Layer Deposition	5
DC	Direct Current	5
Tnws	Titanium Oixde Nanowire Arrays	8
DSSC	Dye-Sensitized Solar Cells	9
Sams	Self-Assembled Monolayers	10
T-BAG	Tethering By Aggregation And Growth	10
THF	Tetrahydrofuran	11
EWOD	Electrowetting-On-Dielectric	12
PFDPA	1H, 1H, 2H, 2H-Perfluorodecyl Phosphonic Acid	15
DI	Deionized	15
ODPA	Octadecylphosphonic Acid	22
FE-SEM	Field Emission Scanning Electron Microscope	24
ATR	Attenuated Total Reflection	25
FTIR	Fourier-Transform Infrared Spectroscopy	25
DRIFTS	Diffuse Reflectance Infrared Fourier Transform Spectroscopy	25
EDX	Energy Dispersion X-Ray Spectroscopy	30
FTO	Fluorine-Doped Tin Oxide	35
UV-Vis	Ultraviolet–Visible	35
NP	Nanoparticle	39
PDMS	Polydimethylsiloxane	39
LM	Light Microscope	41
Astm	American Society For Testing And Materials	42
UV	Ultra-Violet	43

Chapter 1. Introduction

1.1 The Current Physics Model of Wetting

1.1.1 The discovery of superhydrophobicity in nature

Nature is a great vault for scientists and engineers to get knowledge from. “Live in silt but not sullied”, is a line from the Song dynasty Chinese poet, Zhou DunYi (1017-1073), describing his appreciation of the lotus leaf being clean, even though it was grown in mud. The fascinating self-cleaning property is simply amazing and elegant in the poet’s eye. No doubt this interesting physical phenomenon has drawn scientist's attention even after thousands of years. In 1997, two German scientists W. Barthlott and C. Neinhuis tested approximately 340 plant leaves for their water resistant properties by measuring the water contact angle (WCA), followed by taking scanning electron microscopy (SEM) images of the microstructure of the leaf surfaces. They found out that several kinds of plant leaves have similar water repelling properties to the lotus leaf. After careful investigation, it turned out that all leaves which are water repelling have “papillose epidermal cells”, which is covered by a layer of “epicuticular waxes”[1]. This combination provides a superhydrophobic surface that is described by the so-called Cassie-Baxter state, where the liquid is in minimum contact with the surface to maintain thermodynamic stability.

1.1.2 Young’s Equation

The origin of the liquid-solid interaction at an interface can be traced back to the 19th century, when the famous physicist Thomas Young proposed his equation, which would be later known as Young's equation, to describe this interaction. To obtain Young's equation, one can start by deriving the energy changes from when a free droplet in air becomes a stable form on the solid surface. Assuming a smooth surface, one can represent the change of surface energy by the change of the liquid-solid contact angle, known as Θ_Y, and this leads to the Young's equation. A common confusion that arises when deriving the surface energy is that the concept is expressed by surface tension, represented as force vectors in Figure1(a). The surface energy and the surface tension are two interconnected concepts. Surface energy, expressed in $\frac{J}{m^2}$, represents the energy difference between the bulk and the surface; whereas surface tension is the force acting on a line can be seen as a force version of surface energy, as they both express the cohesive force that is binding the atom at the surface, it is safe to say that they are actually identical concepts, which also can be shown when after some units conversion that the unit of surface energy $\frac{N}{m}$ is equal to $\frac{J}{m^2}$, the unit of surface tension.

$$\cos\Theta_Y=(\gamma_{SV}-\gamma_{SL})/\gamma_{LV} \quad (1)$$

As demonstrated in Figure1(a), where "S" stands for solid, "V" stands for vapor, "L" stands for liquid, γ is the change of surface energy per unit area of the medium. Hence, "γ_{SV}" is the change in surface energy between solid and vapor, "γ_{SL}" is the change in surface energy between solid and liquid, "γ_{LV}" is the change in surface energy between liquid and vapor [2]. The main reason

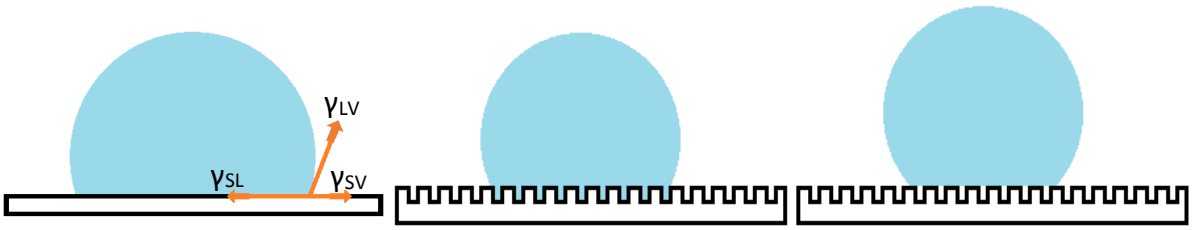

Figure 1. (a)The contact angle derivation. (b)Left, Wenzel type wetting model, right, Cassie-Baxter type wetting model

why Young's equation is so powerful is that by only measuring the contact angle, one can deduce the energy balance at the three-phase boundary, and the liquid-solid interaction is resolved by knowing only the contact angle. However, the equation assumes that the solid surface is perfectly flat and chemically homogenous, which may not very practical.

1.1.3 Wenzel and Cassie-Baxter state

It is not until 1936 and 1944 when Wenzel, then Cassie and Baxter published two different models [3, 4], later known as the Wenzel state and the Cassie-Baxter state, that address the apparent contact angle on a non-ideal porous surface in different conditions. This resolved a lot of questions about the interaction between a non-ideal porous solid surface and liquid. The Wenzel state describes the situation when a droplet fully wets the porous surface while the Cassie-Baxter state acts as a counterpart which describes when a droplets does not wet the porous surface but rather encapsulates the air in the pores. Both of the two models have integrated the roughness term into Young's equation. In the Wenzel state (figure 1b), the modified Young's equation is

$$\cos\Theta^* = r\cos\Theta_Y \qquad 2$$

Where $\cos\Theta^*$ r stands for roughness, which is defined as the ratio of the projected surface area, and the total surface area. In Cassie-Baxter state (figure 1b), the modified Young's equation is

$$\cos\Theta_{CB} = f_s(r\cos\Theta_Y + 1) - 1 \qquad 3$$

Apart from incorporating the roughness factor r, the Cassie-Baxter state introduce the parameter f_s which represents the area fraction of a material in contact with the liquid, which is meant to be applied on surfaces that are formed by multiple phases of materials, or a surface that consists of

different surface energy areas. This rule can be generalized to n distinguishable phases, as the fraction of all different phase will always add up to be 1. The Cassie-Baxter state equation in this case can be generalized to

$$\cos\Theta_{CB}=\sum_i^n f_I(\gamma_{i,SV} - \gamma_{I,SL})/\gamma_{LV} \quad (4)$$

In the real world, the two-phase system is the most frequent encounter. For example, a naturally occuring two-phase Cassie-Baxter state is the previously mentioned lotus leaf scenario, where the surface is considered a combination of papillose lotus leaf cell and an air gap between them. In this case, one can apply equation 3, which is a simplified two phase expression.

1.2 Titanium Oxide Nanostructure-Based Superhydrophobic Surfaces

1.2.1 Overview of Recent Research Trends on Hydrophobic Surfaces

There are numerous reports [5-11] on superhydrophobic surfaces, where approaches and potential applications were plentiful. Generally speaking, in the last decade, research of the superhydrophobic surface is largely inspired by biology, due to the synergy between the structure and chemical composition of things found in nature. Some other naturally found superhydrophobic surfaces other than the lotus leaf have been closely studied, such as Gecko feet, water strider feet, beetle shells, rose petals, mosquito eyes, and the list goes on [5-11]. Approaches such as layer-by-layer formation, electrochemical reaction, sol-gel, photolithography, chemical vapor deposition (CVD), physical vapor deposition (PVD), and electrospinning have been reported [12].

1.2.2 Overview of TiO_2 as a Material

TiO_2 is a very common material found in nature. The naturally occurring ores contain mainly rutile TiO_2, which the most stable phase of the three crystal structures of TiO_2 found in nature. The other two are named anatase and brookite. Traditionally, a sulfate process was implemented to produce TiO_2, which was then replaced by a chloride process due to pollution and economic issues [13].TiO_2 is also a widely used pigment that appears in paints, polymers, printing, and make-up products [14]. TiO_2 is also known to be bio-compatible, the United States Food and Drug Administration (FDA) approves that TiO_2 can be added to a food when weight of TiO_2 is below 1% of the total weight of the food [15]. With a relatively wide-bandgap at around 3.2eV for anatase and 3.0eV for rutile, all crystal forms of TiO_2 are considered a semiconductor, which is appropriate for use in solar cells and photocatalysis applications.

1.2.3 Introduction to Electrochemically Formed Titanium Oxide Nanostructures

As fast growing nanoscience has shown great potential in a vast number of research areas, the increasing surface area of nano-sized structures is a core concept that seen in many nanoscience applications. The advantage of high surface area in many nanomaterials has led to numerous breakthroughs and discoveries in many fields: catalysis, optics and surface chemistry; and applications including battery electrodes, supercapacitors, solar cells, sensors, and self-cleaning surfaces.

1.2.3.1 Electrochemically Anodized Titanium Dioxide Nanotube Arrays (TNAs)

The self-organized TNAs are one of the most exciting nanostructures known. The growth mechanism is simple yet effective. The most remarkable advantage of this process is the ability to precisely control the dimensions and order of the nanotubes. Compared to earlier approaches to make TiO_2 nanotubes, such as sol-gel and atomic layer deposition (ALD), electrochemical anodization demonstrates far more superiority in control of the growth. The process needs only a pair of electrodes, a direct current (DC) power supply, and a reaction chamber with electrolyte. Such a simple set-up offers great potential towards scalability and industry application. The as-formed TNA provides a self-arranged "honey comb" like nanostructure, which is ideal for a Cassie-Baxter state superhydrophobic surface.

In electrochemistry, the electrochemical anodization process is the dissolution of the anode metal and the subsequent formation of oxide layer. Theoretically, three possibilities of reaction can occur when a metal is in the anodization set up (Figure 2d). One possibility is that the anode starts to dissolve into the solution as the reaction starts; the second possibility is that the metal forms an oxide at the surface and the reaction is stopped; the third possibility is that the process of dissolution is in competition with the process of oxidation. The ordered nanoporous and nanotube array structure is obtained from the third possibility. It was first demonstrated in industry on aluminium alloy as early as 1923, as a method for anti-corrosion [16]. Today, such a method is a widely used as a pre-process of dyeing. Products such as the Apple iPhone series, which are equipped with an aluminum back case has an anodic aluminum oxide layer at the surface filled with dye [17]. Electrolytes such as chromic acid with hydrofluoric acid were used at first. Many improvements have been made since then [18-20]. It was also demonstrated that

using organic electrolyte instead of water, such as ethylene glycol, will reduce the side wall "ripples" and grow longer nanotubes [20].

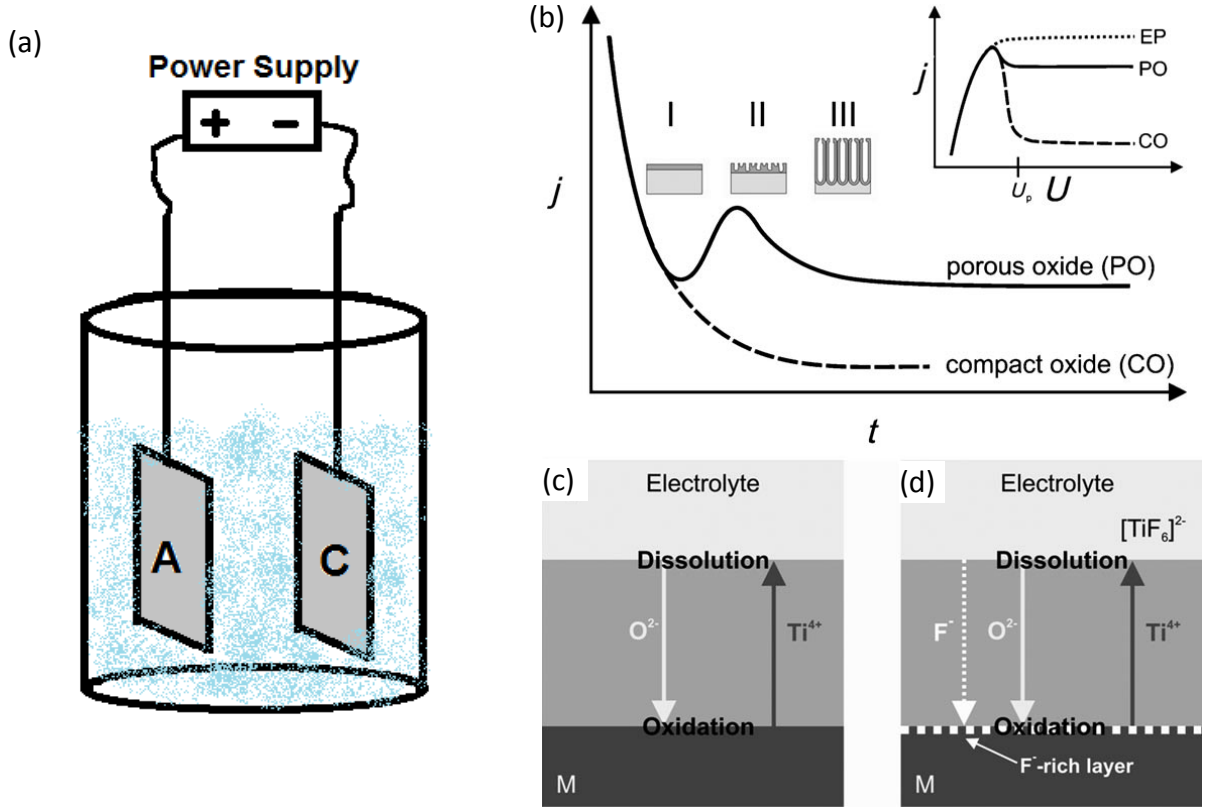

Figure 2. a) Drawing of an anodization setup. b) Typical current vs time plot for an anodization process. Solid and dashed lines represents the presence and absence of F^- ions, respectively. A compact oxide layer is obtained when there is no F^- ions as opposed to a honeycomb/tube-array structure is obtained with F^- ions. The honeycomb/tube-array structure has a three-stage formation process. Inset is a current potential plot, where the dot lines, solid lines, and the dashed line represents a high F^- content electrolyte, a medium F^- content electrolyte, and a low F^- content, respectively. c) d) are reaction mechanism for field assist ion transport during the anodizing, where in c) the electrolyte is F^- free while d) has F^- ions. (Modified with permission from Angew. Chem. Int. Ed. 2011, 50, 2904 – 2939. Copyrights, 2001 Wiley and Sons).

In a typical anodization process, if the current (j) is plotted versus time (t), a graph similar to figure 2(a) can be obtained. The graph shows there are three stages in nanotube growth, which are distinguishable through the change in current. Figure 2 (b) and (c) shows the difference of reaction mechanism for with or without F^- ions. A thick oxidation layer is formed when applying a positive bias at anode in an F^- ion free environment, and a very low current is observed and will gradually decrease to zero when the layer is thick enough so the field cannot penetrate anymore. On the other side, when F^- ion is present in the electrolyte, the Ti^{4+} ions can react with F^- ions to

form $[TiF_6]^{2-}$ which is soluble, so the formed oxidation layer will become porous as Ti migrates to the electrolyte by this mechanism. As the dissolution of Ti^{4+} and the oxidation of Ti is happening simultaneously, the layer keeps deepening as times goes by, and eventually forms deep pits that are tubular shaped, in other words, the TNAs.

1.2.3.2 Hydrothermally Formed Titanium Dioxide Nanowire Arrays (TNWs)

The history of hydrothermal synthesis can be traced back to 1800s, where the term was first used by Sir Roderick Murchison from UK [21]. The early contribution was mostly dedicated to the synthesis of quartz crystals, of which the main reason is to simulate the environment in the earth's crust, where natural quartz is formed. Small amounts and fine grains of quartz products, however, are all being discarded due to there being no electron microscope available for investigating micro- or nano-sized crystals [22]. The process of hydrothermal synthesis including placing a mineralizer, mostly water (giving it the hydro- suffix), along with compounds that contain the elements of targeted products in a heated (-thermal) autoclave, also known as a "hydrothermal bomb" named by Friedel and Sarasin [23], to react under pressure and heat. At first, the majority of reactors were made of glass tubes. To perform synthesis at higher temperature, the steel reactor was introduced, and soon noble metal lining was introduced to prevent corrosion of the reactor [24]. According to the historical summary of hydrothermal synthesis by Byrappa and Yoshimura, it was not until 21st century that the hydrothermal method is used for nanomaterial synthesis [22].

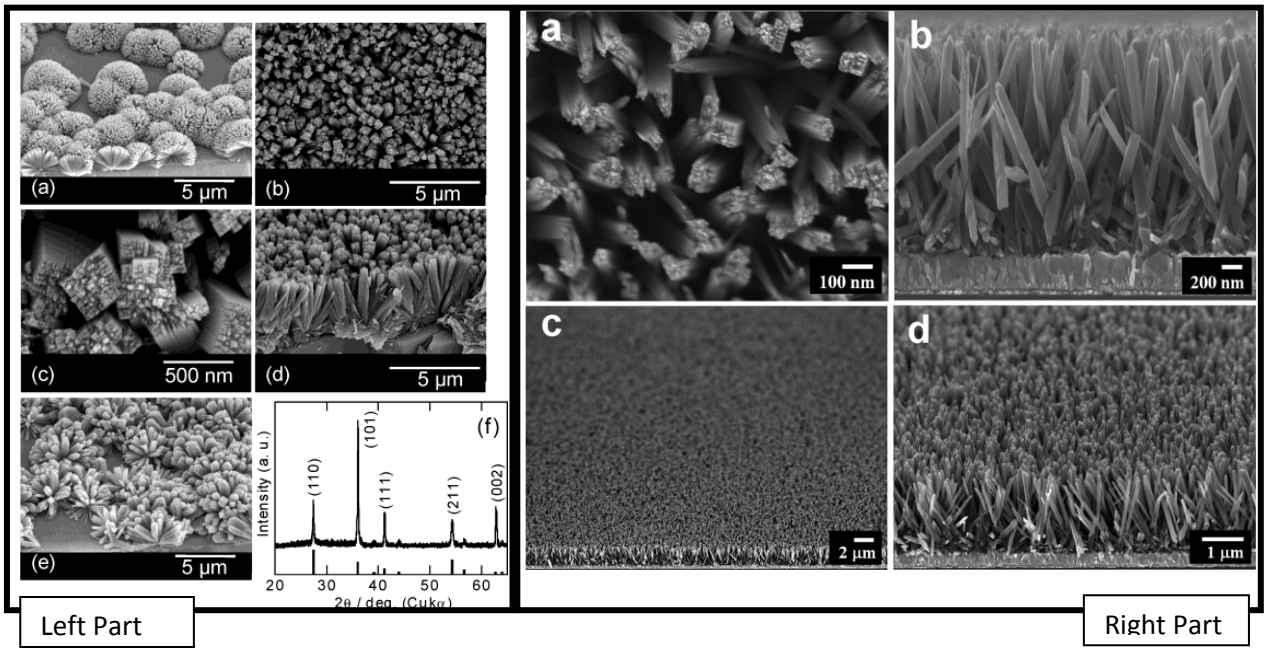

Figure 3: Left Part, SEM micrographs of nanowires prepared by Hosono et al. Right Part, the TNWs prepared by Liu et al. Adapted with permission from Hosono, E.; Fujihara, S.; Kakiuchi, K.; Imai, H. J. Am. Chem. Soc. 2004, 126, 7790–7791.Copyright 2004 American Chemical Society. (Left Part)(25) Adapted with permission from Bin L and Eray A. J. Am. Chem. Soc. 2009 *131* (11), 3985-3990. Copyright 2009 American Chemical Society. (Right Part) (29)

The first report of hydrothermal synthesized TiO_2 nanowire arrays is prepared by Hosono et al. at early 2004 (Figure 3 left part) [25]. Later in 2004, a more ordered structure is reported by Weng et al.; however, a polymer-TiO_2 seed layer was used to assist the growth of TiO_2 nanorods and it might be questionable to say it is a hydrothermal process since the reaction is at atmosphere pressure [26]. The nanowire arrays obtained by Hosono [25] is rather a cauliflower-shaped crystal (figure 3 left part), where the nanorods are "pedals" of the cauliflowers that grow into each other after a period of time. Though improved in control of orientation and shape, the later work from Feng et al. [27] and Kakiuchi et al. [28] still has only flower shaped nanowires. As the rise of research in Dye-Sensitized Solar Cells (DSSCs) continued, more transparent, ordered structures were demanded. Liu et al. successfully synthesised almost vertically orientated TNWs in 2009, aiming to provide an electron transport layer in the DSSC (Figure 3 right part) [29]. Finally in 2010, Kumar et al., showed that TNWs can be prepared on multiple types of substrates [30]. Hydrothermally formed TNWs have a different surface texture

compared to the TNAs. The TNW surface is full of open pores and is optically transparent. One of the most important advantages over other growth methods is that the TNWs can be easily grown on non-native surfaces, i.e., substrate material is not the same as the material growing on top of it. For example, a TNW grows a non-native substrate means the substrate is anything but Titanium. Usually, hydrothermally grown TNWs are grown on glass or FTO glass substrates since it is necessary in solar cell research.

1.3 Introduction to Self-Assembled Monolayers (SAMs) and Their Role in Surface Modification Processes

It is necessary to understand the concept of SAMs because this is the common method used to alter the surface energy of TiO_2 in order to achieve the Cassie-Baxter superhydrophobic state. In short, the SAMs on TiO_2 function the same as the wax on the lotus leaf. SAMs are not limited to molecules, any organic molecule that can be packed as a single layer on a surface can be considered a SAM, the often-used analogy is a layer of hair that grown on skin. The process of growing a SAM on a surface is called functionalization. Common characteristics of a SAM molecule are long chains, with a specific functional group (thiol, carboxylic acid, phosphonic acid, etc.) at one or both ends.

The development of SAMs was first inspired from the Langmuir-Blodgett films where it was discovered that if a small amount of a surfactant that has a hydrophilic end group at one side and a hydrophobic end group at the other side was mixed in water, they will line-up and form a film at the air-water interface. Exposing the hydrophobic group to air and the hydrophilic group to water. If a hydrophilic surface was inserted vertically in the water, then drawn back slowly, the as-formed film will be transferred to the solid surface. An example in daily life is the oil film on

soup, if a bread crust is being dipped in the soup and taken out right after, it will keep that film intact on its surface. What distinguishes SAMs and Langmuir-Blodgett films is that the surfactants are physisorbed to the surface as a Langmuir-Blodgett film but chemically bond to a surface when it is SAMs which is also called functionalized (Figure 4). Bigelow et al. demonstrated SAMs of eicosyl alcohol ($C_{20}H_{41}OH$) on a metal surface in 1945, which is considered a pioneer demonstration [31]. Later head groups, namely chlorosilane, alkanethiol, phosphonic acid, were developed, benefitting from Bigelow's discovery. Functionalization processes usually involve immersion of a surface in the solution that contains the monomers,

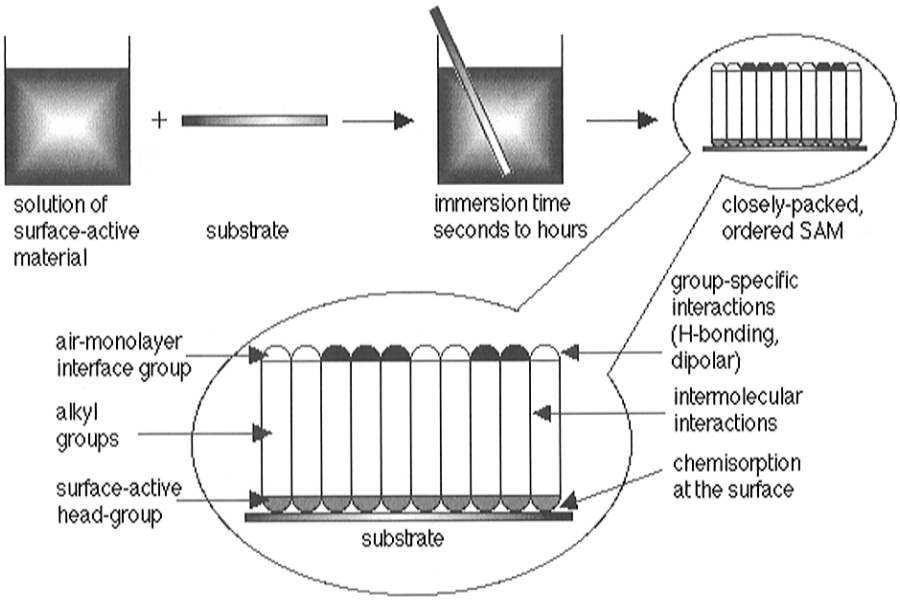

Figure 4: Immersing method formed SAMs. SAMs will formed on the surface due to spontaneous heat motion when immersed in a non-polar solution. Reprinted with permission from Chem. Rev. 1996, 96, 1533−1554. Copyright 1995 American Chemical Society.[32]

where the surface was taken out of the solution after a period of time. Other than immersion, a quicker method called "T-BAG" (tethering by aggregation and growth) that utilized the evaporation of the solution and the concept of a Langmiur-Blodgett process, was introduced in 2003 by Hanson et al. [33]. Solvents are usually non-polar, such as ethanol, methanol, 2-propanol, hexane, toluene and tetrahydrofuran (THF) [34-37].

To characterize the quality of SAMs, contact angle measurement is one of the common methods used. For example, a hydrophilic surface that is functionalized by a SAM has a hydrophobic end group which will become hydrophobic after. The change in surface tension by SAMs also draws interest in research of superhydrophobic/superhydrophilic surfaces, with potential applications in water repelling, anti-fogging [38], anti-icing [34], and drag reduction surfaces [39].

1.4 Introduction to Superhydrophobic Coating Based On Nanoparticles

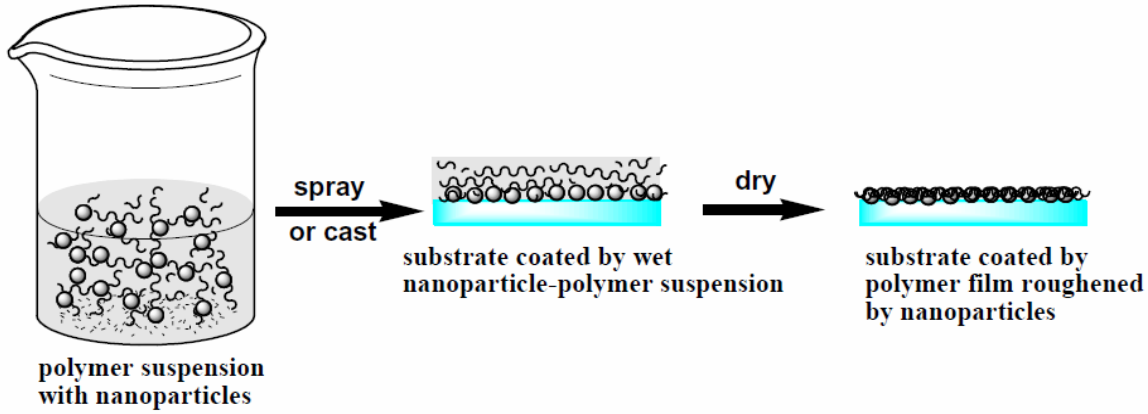

Figure 5: The process of producing the nanoparticle-polymer blend based superhydrophobic coating. © 2010 National Institute for Materials Science[40]

In some processess, both hydrothermal and electrochemical anodization processes are not possible to perform to obtain the nanostructure in order to produce superhydrophobic surface, especially in industry applications where a large surface area is required. This is why a coating technique is introduced to diversify the applications of TiO_2 superhydrophobic surfaces; since a coating is also considered a very practical approach for industry applications due to its adaptability. A common method to obtain a coating is through spraying or brushing of a liquid. In order to obtain roughness and durability, the liquid is usually contained with a mixture of particles and polymers. For example, Steele et al. reported a coating based on ZnO nanoparticles and perfluoracrylic polymer [40]. When applied, the particle formed a self-arranged structure

that is rough and has a micro-nano hierarchy. After drying, the polymer acts as a glue to hold the rough structure and make the coating robust. As shown in figure 5, the process allows the nanoparticles to act as a film roughening agent, which results in a rough, low energy surface.

1.5 Introduction of Electrowetting-on-Dielectric (EWOD)

Electrowetting is a phenomenon that describes the change in wetting of a liquid under an applied electric field. The very first known demonstration is the Gabriel Lippmann's experiments at 1875 [41]. Lippmann's equation (equation 5), also called the Lippmann-Young equation, gives a clear expression of how voltage will change the contact angle.

$$\cos\Theta=\cos\Theta_o+\frac{1}{2\gamma_{LV}}CV_e^{\,2} \qquad 5[41]$$

$\cos\Theta_o$ is the contact angle when there is no voltage applied across the interface. C is the capacitance of the dielectric (acting as a planar capacitor), and V_e is the applied voltage. EWOD is one type of setup of Electrowetting where a dielectric layer is in between the droplet and the electrode substrate, also called "actuation electrodes" [42, 43]. Figure 6 is an illustration of how the charges in the liquid change with and without application of a voltage. The main principle is that the charge in the dielectric is relocated to the interface when a voltage is applied, the charge in the liquid will accumulate to the surface as well, due to the Coulombic attraction. Traditional electrowetting is based on a metal-liquid system, where the electric double layer (EDL) is acts as the capacitor between the liquid and the solid (shown in Figure 6 left part).

According to Wyatt et al., the two greatest advantages of EWOD over the traditional electrowetting setup is that first, the dielectric layer between the droplet and electrode counteracts the electric field so that a higher voltage can be applied; thus a stronger electrowetting effect can be obtained.

Secondly, a hydrophobic layer with small contact angle hysteresis can be applied so that the droplet can be moved on the surface [44]. Actuation of small droplets, such that the size is below the capillary length was realized in the 1980s. However, as Wyatt et al. mentioned, it was not until 2002 that the first successful droplet transport on an EWOD device was reported by Lee et al.[42, 44].

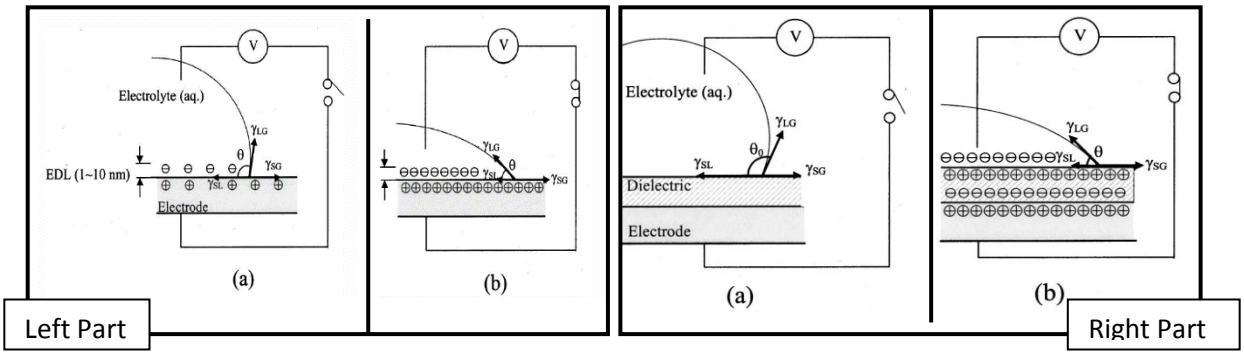

Figure 6: Left Part, schematic of changing of the water contact angle of a traditional electrowetting device without a bias, (b), with bias. Right Part Schematic of changing of the water contact angle on a EWOD. (a) Without a bias, (b) With a bias. The field drives the reduction in contact angle as shown in (b). Reprinted from, with the permission of AIP Publishing.[45]

Chapter 2. TNAs Based Superhydrophobic Surface and Relation between Length of Nanotubes and Hydrophobicity

2.1 Introduction to TNA-Based Superhydrophobic Surface

Inspired by the lotus leaf effect, superhydrophobic surfaces with self-cleaning functions are of particular interest to researchers. TNA-based superhydrophobic surfaces have about a decade of history so far. Many [35, 46-48] have reported superhydrophobic surfaces based on TNAs. Usually, functionalization with hydrophobic SAMs is a necessary process to achieve superhydrophobicity due to TiO_2 having an otherwise superhydrophilic nature. The nanostructure of the surface contributes to the surface roughness needed to achieve the Cassie-Baxter state. In general, a rougher surface or a more porous surface will be more hydrophobic. However, there are still other factors; for example, the air pockets formed in the nanotubes under the water droplet, the tube diameter, the length of the tubes, and the tube to tube distance all affect the hydrophobicity of the surface in different manner, and their contributions are still unclear. We experiment on how the length of the nanotubes will affect the hydrophobicity of the functionalized TNA surface, and the result is compared to a theoretical model to analyze possible discrepancies and the physics behind them. In addition, the variation in water adhesion of the TNAs at different lengths is also analyzed.

2.2 Preparation of Superhydrophobic TNAs

2.2.1 Materials Used

1H, 1H, 2H, 2H-perfluorodecyl phosphonic acid (PFDPA) with the molecular structure $CF_3(CF_2)_9(CH_2)_2PO_3H_2$ was supplied by Aculon Inc. Methanol (99.8%), acetone (99.5%), ethylene glycol (99.9%) and ammonium fluoride (98.3%) were obtained from Fisher Scientific. Deionized (DI) water used for contact angle measurements was obtained from FTA-200 system. Titanium foil (99.9%) was supplied by Alfa Aesar.

2.2.2 Preparation Procedure

TNAs were prepared by electrochemical anodization at room temperature using a two-electrode setup. Prior to anodization, titanium foil was degreased ultrasonically in acetone, methanol and DI water for 10 minutes each. A 1*4 Ti foil was immersed in the electrolyte by an O-ring and formed the anode; the cathode was a piece of titanium with a surface area that is half of the anode Ti foil. The anode and cathode were set to be 3.5 cm apart. A DC power supply (9312-PS Variable Benchtop Power Supply, MPJA Inc.) was used to drive the reaction. The electrolyte was 0.3 wt% NH_4F, 4% DI water in ethylene glycol. The Ti foil was anodized at 60 V, while the span of anodization ranged from 10 minutes to 3 days. Meanwhile, TiO_2 planar thin films were prepared by annealing Ti foil for about 4 hours on a hot plate at 225 ºC. To functionalize, Hydroxylated TNAs and TiO_2 planar thin films were immersed in 1 mM solution of PFDPA in methanol for 24 hours. The resulting contact angle is listed in figure 7.

2.3 Results and Discussion

2.3.1 Contact Angle Measurements

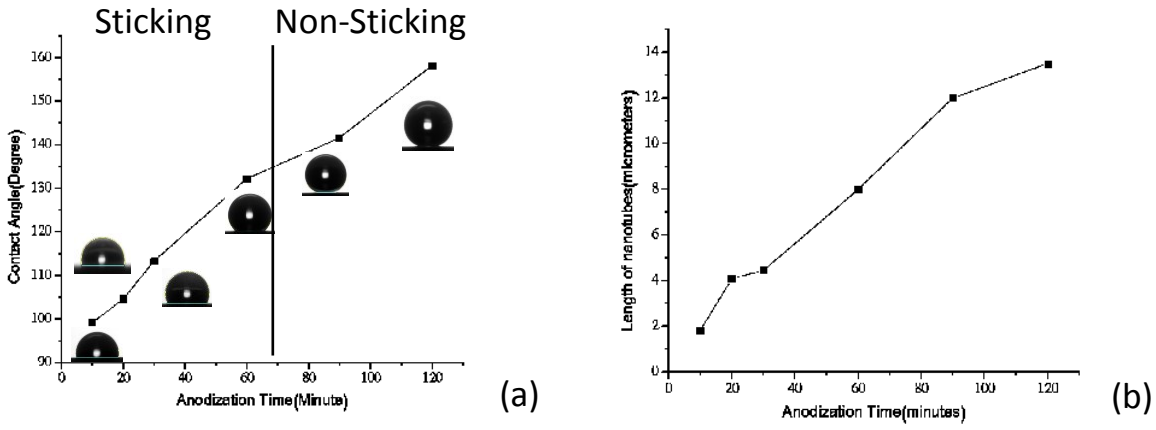

Figure 7: (a) The relation between anodization time and contact angle after functionalization. (b) The relation between length of nanotubes and anodization time.

The resulting contact angle with regard to anodization time of TNAs is shown in figure 7(a), and the length relation to anodization time is in figure 7(b). The contact angle is increasing with the length of the TNAs. An initial interpretation of this relation is that the air encapsulated in the nanotubes is being pressurized and exerting a repulsion force to the water droplet. As the length increase in TNAs, the air volume encapsulated in the nanotube is increased as well. Consequently, the resulting repelling force is increasing and so does the contact angle, as the water feels a repelling force from the surface.

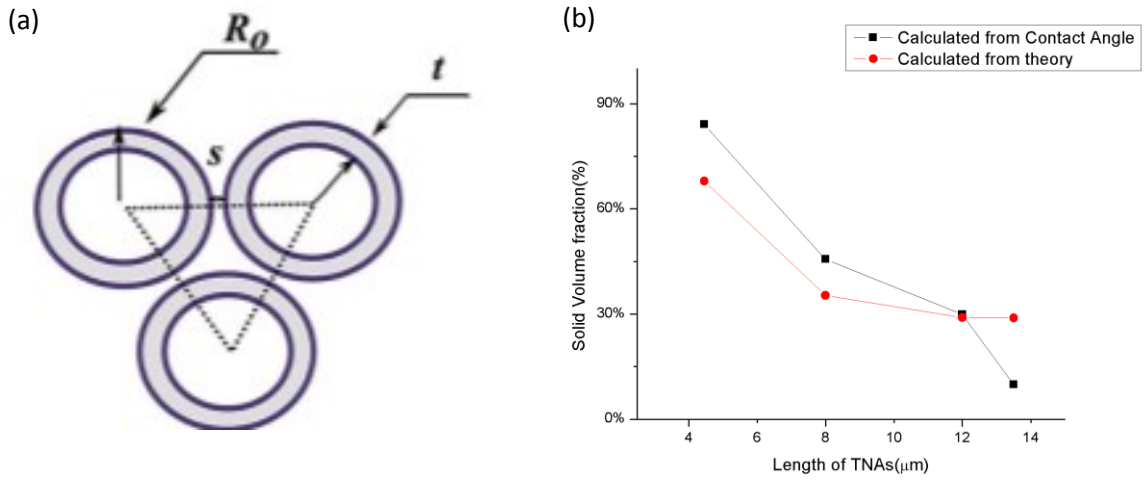

Figure 8: The TNA surface area calculation model derived by Farsinezhad et al. Reproduced from [35] with permission of The Royal Society of Chemistry.

However, other observations shows that the air pressure is not the only reason for the increase in contact angle with the length of TNAs. First, the contact angle measurement does not fall into the prediction of the theory. Farsinezhad et al. [35] proposed a model for calculation of the contact area of liquid on the TNA surface as shown in figure 8a, where it is assumed that all the nanotubes are closed packed, with a fixed inter-tube distance; the "unit cell" of this model is a triangle made from three of the packed tubes [35]. This model is somewhat accurate but lacking considerations towards the variation of tube wall thickness and inter-tube distance in real cases. To know the solid surface contact fraction, the geometry model by Farsinezhad et al. is used, while the tube diameter, wall thickness, and inter-tube distance are obtained from SEM images of real samples. The wall thickness of nanotubes at different lengths are measured from SEM images in Figure 9, using pixilate software. It is known that the wall thickness will change with the anodization time, and the TNAs are v-shaped after a relatively long time of anodization [49]. Therefore the surface solid area fraction changes with the growing tube length. It is explained by Macak et al. [20] that the diffusion of the $[TiF_6]^{2-}$ ions plays a significant role in variations of inter-tube distance because

the inter-tube gap comes from the dissolution of the $[TiF_6]^{2-}$ ions. In addition, varying the anodization voltage, electrolyte content (eg, HF as a source of F^- instead of NH_4F), and inter-electrode distance will also change the inter-tube distance of the obtained sample since all these conditions will affect the generation and diffusion of $[TiF_6]^{2-}$ ions. However, according to the images at tube length beyond 8 μms, the wall thickness of the nanotubes does not change much (~5%); thus the total surface area fraction does not decrease much with further increasing of TNA length (to 20 μms or more) under the same experimental conditions. The two data lines represent the solid surface area fraction is plotted in figure 8b, with one calculated from the Farsinezhad's model, using tube sizes from SEMs in Figure 8 (with round markers), and the other one calculated from the Cassie-Baxter model using the measured contact angle data from the same samples (with square markers). The two data differentiate when the TNA length is more than 12 microns. Surface area calculated from contact angle data drops to less than 10% when the length of TNAs reaches about 14 μm, which indicates the surface area of the TNAs is decreasing further with the increasing the length. However, the SEM image already shows that the surface area decreases no more at 12 μm. The reason could be that there are some other factor that is missed in the model. Figure 8d inset includes some good examples of these missing factors. They are the gaps that appear among the TNAs, which are generated during the process of removing the debris layer of the as-anodized TNAs. According to the SEM image, the longer the nanotubes the more gaps there are. Theoretical models assume closed packed nanotubes while in this case there are gaps that are not in the model, when more gaps appear at the surface, the surface area will deviate more from the theoretical model, despite the tube diameter being stable when length is more than 12 μm.

2.3.2 The Sticking Surface versus Non-Sticking Surface

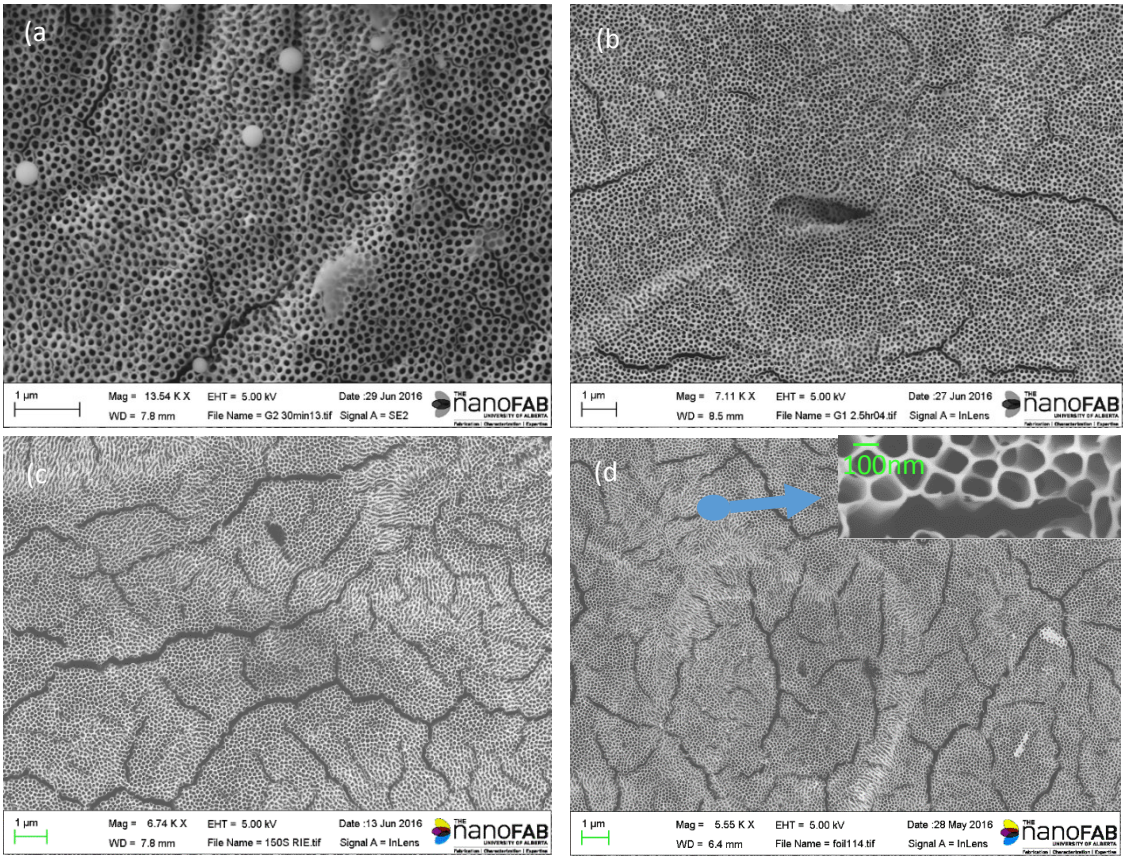

Figure 9: (a) 30min anodization, 5 µm TNAs (b) 1 hour anodization, 8 µm TNAs (c) 1.5 hours anodization, 12 µm TNAs (d) 2 hours anodization, 14 µm TNA. Inset: and the zoom-in view a random picked area, the yellow shaded areas indicate some of the "missing areas"- the gaps generated from the process of removing the top debris layer of the TNAs.

The second discrepancy comes from the stickiness of water on the surface, as demonstrated by Lai et al. previously [50], the water stickiness of TNAs depends on the ratio between the open and closed air pockets. Open air pockets will make the surface less sticky and the closed air pockets will make the surface stickier. Lai et al. [50] also mentioned that the capillary force is the dominating force that acts to hold the droplet. This theory predicts that when the nanotubes grow longer, they are better at holding the droplet, since longer tubes will encapsulate more air, thus higher pressure difference between the inside and outside of the tube. However, the TNA surfaces that are shown above have experienced a sticking to non-sticking trend with the length.

The cut off is at 12 μm in length (1.5 hours equivalent anodizing time). The 8 μm length (1 hour equivalent anodizing time) TNA surface holds water droplets even when flipping over (180 degree). However, when the length reaches 12 μm and more, the water droplet will slide off at relative small roll-off angle, and the angle decreases as the length increases. This phenomenon disagrees with the model suggested by Lai et al. [50] at the first glance. As it is stated by Lai that the higher volume of air trapped in the structure, the higher the excess pressure there will be, thus a stickier surface is obtained; but the water droplet does not stick to the longer TNAs at all. As the microstructure is what changes the stickiness of the surface, SEM images in figure 9 provide insights to this observation. It can be seen that when TNAs grow longer (5 to 14μm from (a) to (d) under the same growing conditions), more gaps are appearing with a wider opening of each gap. The reason for the appearance of the gaps is suspected to be the grain boundaries of the substrate; or that they grow during the anodization process due to the release of the local stress in the material driven by thermodynamics. It is proposed that the gaps between the "packets" of nanotubes are acting as open air-pockets that free the droplet from the pinning of the closed air-pockets, as more and wider gaps opening up, the surface become less sticky due to more open air-pockets being present, based on Lai's theory [50].

Functionalization on short TNAs on non-native substrates is also performed. The substrate is an FTO slide, with 500 nm of Ti sputtered on top. The TNAs are obtained by anodizing the sputtered layer. The result is a close packed, thick-wall TNA. The highest WCA achieved by this method of surface functionalization is 130°. There are two main reasons for the lower contact angle compared to a TNA on native substrate. Firstly, due to short length of TNAs, less cracks are formed resulting in a higher solid contact area fraction, which is explained previously. The second reason is a minor effect but should not be ignored, which is the morphology of Ti. The

native Ti foil is thick and rough while the sputter grown Ti is much smoother (mirror like) than the foil. So even if a thicker Ti is sputtered, it is not likely that the sputtered Ti will form large cracks similar to those which appeared in the Ti Foil due because it has much finer grains.

2.4 Conclusion

We have shown that the length of TNAs has some relation with the WCA after functionalization. However, the length of the TNAs only affect the WCA indirectly, through its influence on the surface structure. It is revealed that during the debris layer removing process, long irregular shaped gaps appear on the surface of the TNA, at micron scales. Different TNAs have shown different levels of gap openings and density. Longer TNAs generates more and larger gaps between the "packets" of TNAs, and it is the gaps what provides more air fraction at the surface thus leading to a higher WCA. These gaps between packets of TNAs, or in other words, what made the TNAs into packets, are missing in the consideration of theoretical model, yet play an important role on the contribution to the surface roughness and WCA. In the future, for research on TNA based superhydrophobic surfaces, the surface gaps will be worth some attention and are non-negligible when it comes to surface roughness and WCA measurement.

Chapter 3. TNA-based Ultrasound Resistant Superhydrophobic Surface

3.1 Introduction to Ultrasound Resistant TNAs

Until now, little attention has been focused on the superhydrophobic surface's durability against harsh conditions. Wang et al. [51] verified the stability of a superhydrophobic polybenzoxazine surface in all pH environments. In another work, the longevity of superhydrophobicity on aluminum and its alloys was examined via long time immersion in acidic and basic solutions [52]. Recently, it was found that an Al_2O_3 coating with perfluorodecyltrichlorosilane endowed the surface with excellent mechanical durability and good corrosion resistance [53]. Zhe Cui et al. [54] investigated the effect of high speed current scouring on superhydrophobic surfaces. Apart from this, different kinds of superhydrophobic surfaces have been developed and their robustness has been studied in different environmental conditions [55-57].

3.2 Preparation of Superhydrophobic TiO_2 nanotubes

3.2.1 Preparation of Aqueous Based TNAs

Titanium dioxide nanotube arrays (TNAs) were prepared by electrochemical anodization at room temperature using a two-electrode setup. Prior to anodization, titanium foil was degreased ultrasonically in acetone, methanol and DI water for 10 minutes each. Typically, 1 * 4 cm Ti foil was immersed in the electrolyte and formed the anode; the cathode was a piece of titanium with a

surface area that is 1 x 2 cm, half of the anode Ti foil. The anode and cathode were set to be 5 cm apart. A DC power supply (9312-PS Variable Benchtop Power Supply, MPJA Inc.) was used to drive the reaction. The electrolyte solution was prepared by mixing 0.1M citric acid and 0.1M sodium fluoride (sodium fluoride and citric acid monohydrate was purchased from Fisher Scientific.) and dissolved in DI water. The pH of the solution was strictly maintained at 5 by adding adequate amount of NaOH solution. Thereafter, Ti foil was anodized at 25 V for 15-17 hours. Afterwards, the newly formed TNAs was sonicated in methanol solvent for 5-10 minutes in order to remove the debris layer.

3.2.2 Functionalization

The cleaned TNAs were immersed in 1mM Octadecylphosphonic acid (ODPA) (purchased from Alfa Aesar with 97% purity) and Perfluorodecylphosphonic acid (PFDPA) (purchased from Aculon) solution in methanol (99.8% purity) at room temperature for 18 to 20 hours in order to achieve functionalization. Afterwards, the modified surface was rinsed with methanol to remove all physisorbed molecules and then dried thoroughly with N_2 gas flow.

3.3 Results and Discussion

In this report, a superhydrophobic surface of TNAs has been prepared by coating it with a conformal layer of two different organic molecules, ODPA and PFDPA. An ultrasonic wave

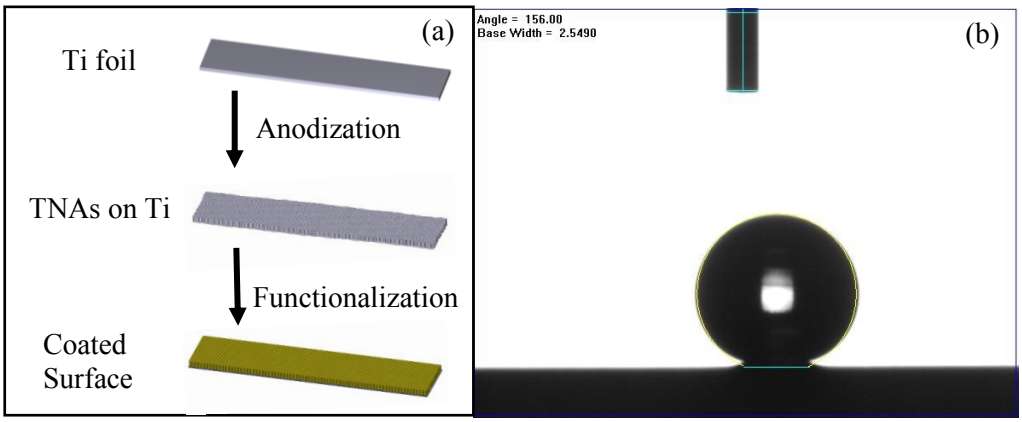

Figure 10: Process flow of TNA fabrication: (a)From top to bottom: The cleaned (Ultrasonicated in acetone, methanol, water, for 10 minutes each) Ti foil before anodization; the TNA grown on the Ti foil in water based electrolyte, ~16 hours growth time, molecular coating is applied to functionalize the surface (PFDPA or ODPA in methanol as the functionalization solution, sample immersed for 24 hours), (b) Example of contact angle measurement shows superhydrophobicity of the functionalized(with ODPA) surface.

method was developed to evaluate the resiliency of the as-prepared superhydrophobic surfaces due to its high contact angle and potential application, especially in making water repelling ultrasonic baths and other industrial purposes. The results corroborate that the water repelling behavior of the two functionalized TNA surfaces is sustained even after the treatment with ultrasonic waves, up to a maximum of 70 minutes at 225 watts. Immediately after 70 minute ultrasonic treatment, the superhydrophobic surface turns into a hydrophilic surface. In comparison between ODPA and PFDPA layer, the PFDPA grafted TNAs show more robustness in terms of contact angle values. Surprisingly, it was noticed that the lost superhydrophobic character, due to ultrasonic wave treatment, is slowly recovered over time while the surface is kept in ambient conditions.

Figure 10 (a) schematically illustrates the stepwise formation of the TNAs followed by passivation with ODPA and PFDPA (example of contact angle in figure 10(b)). This process exploits the well-established affinity of the phosphonic acid functional group to metal and metal oxide surfaces[58]. Evidently, metal oxides that have a nanostructure, such as a TNAs, are better than smooth bare metal oxide surfaces with regard to minimizing the contact area with the water droplet, resulting in a higher static contact angle with nanostructured surfaces [59-61] as expected following the Cassie-Baxter model. Prior to passivation with organic molecules, the morphology of TNAs was characterized by field emission scanning electron microscope (FE-SEM) and figure 11 depicts the relevant FE-SEM images. In our case, the diameter of nanotubes is between 90-100nm and approximately 900 nm in length.

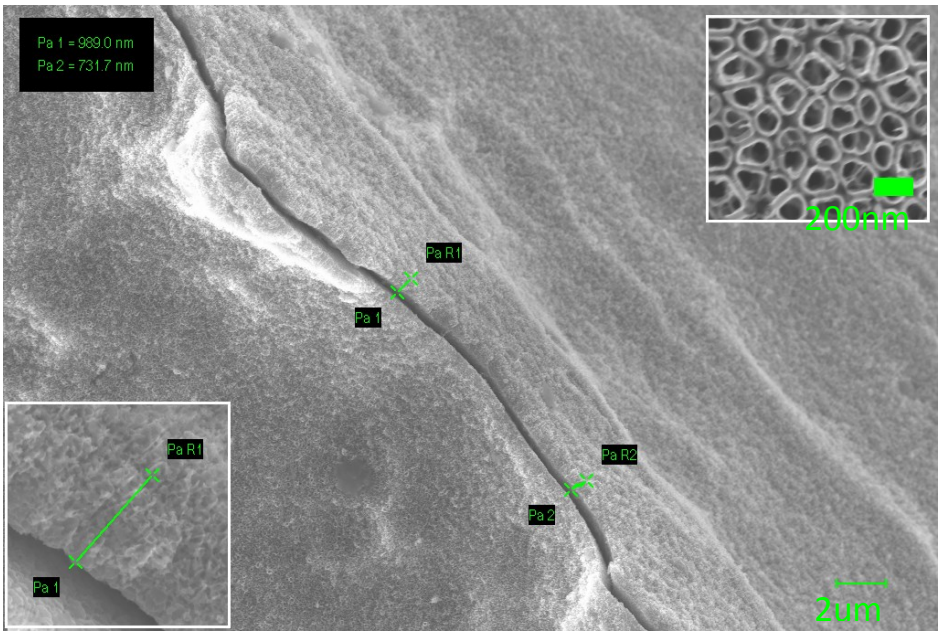

Figure 11: FE-SEM image of the TNAs, the main picture shows the overlook and the edge of the TNA sample that formed on Ti foil, where the top right inset is a zoomed-in view of the TNAs and the bottom left inset is a zoomed-in view of the length of the nanotubes measured from their edge.

In order to confirm the attachment of molecules on the TNA surface, before and after ultrasonication, an Attenuated Total Reflection (ATR) measurement was performed. Figure 12 (a)

shows that the two peaks appear around 2919cm^{-1} and 2850cm^{-1} in fresh samples, attributed CH_2 anti-symmetric and symmetric stretching respectively [61]. However, it was found that the intensity and the shape of these two peaks were completely disrupted because of long time ultrasonic treatment. The sample stayed overnight in the air before the Fourier-transform infrared spectroscopy (FTIR) spectrum of the functionalized nanostructures was recorded a second time (Fig. 12 (b)); surprisingly, the two characteristic peaks of C-H stretching re-appeared at the same position with appreciable intensity. It is very interesting that the two peaks rise again only after being placed in the air overnight. We interpret that this could be due to the packing of the molecules being disrupted by the high energy ultrasound; thus, they show hydrophilicity immediately after ultrasound treatment. The slight shift in the CH_2 anti-symmetric peak from 2919.7 to 2917.8 could be explained by the molecules being misaligned or aligned at a different angle. Once the ultrasound is removed, the organic molecules eventually return to their original orientation. This minimizes their surface energy, re-achieves thermodynamic equilibrium state, and the sample recovers its superyhydrophobic properties. It is worth mentioning that all spectra have been collected by subtracting the blank sample (only TNAs) spectra. On the other side, diffuse reflectance infrared Fourier transform spectroscopy (DRIFTS) was used to confirm the existence of PFDPA molecule on TNAs surface (Fig. 12(c)). The appearance of two peaks for C-F bond stretching around 1210cm^{-1} and 1150cm^{-1} corroborate the existence of the organic molecules on the surface (48). This spectrum was compared with unpassivated TNAs surface in figure 12 (c), where the blank TNA surface shows no distinguishable peaks.

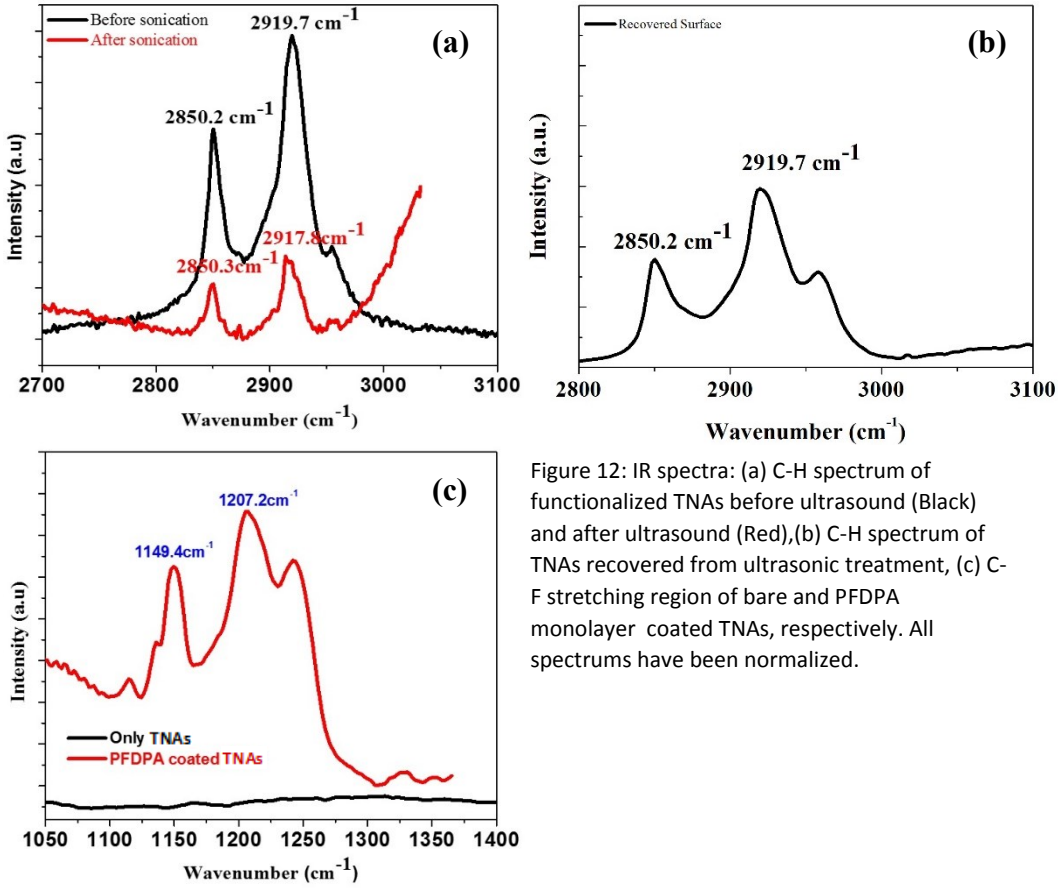

Figure 12: IR spectra: (a) C-H spectrum of functionalized TNAs before ultrasound (Black) and after ultrasound (Red),(b) C-H spectrum of TNAs recovered from ultrasonic treatment, (c) C-F stretching region of bare and PFDPA monolayer coated TNAs, respectively. All spectrums have been normalized.

In the next step, we systematically investigated the static contact angle on bare TNAs, coated (with ODPA and PFDPA) TNAs, coated TNAs right after ultrasound treatment, and coated TNAs placed overnight in an ambient environment after ultrasound treatment. We used the sessile drop technique with 4µL of DI water, where results are presented in Figure 4. We maintain 20 minutes of sonication in each cycle at 225 watts as output power, and the static contact angle was recorded between cycles. To start, the static contact angle value for bare TNAs was found to be 18° (figure 13(a)), which is quite apparent because bare TNAs are known to be superhydrophilic [62, 63]. The ODPA and PFDPA coated TNA surfaces displayed contact angle ≥ 150° (figure 13b and c), but it was difficult to put a water drop on a fresh passivated TNA surfaces because of their water-repelling properties and therefore difficult to measure a more accurate value. The high value of contact angle for both surfaces was maintained even after 3 cycles of ultrasonic treatment.

However, after 3 cycles of ultrasonication, some parts of the surfaces, especially at the edge, started to become hydrophilic, but the central area contact angle (for ODPA coated 148°) was consistently superhydrophobic. The same observation was noticed for ODPA and PFDPA coated surface. Afterwards, both the passivated surfaces were further sonicated for another 10 minutes under the same conditions. Consequently, the main area contact angle decreased dramatically and appeared at 85±3° (figure 13e). Fascinatingly, while the contact angle was measured in the following day for both the samples; the contact angle returned to 125±5° of the original ODPA coated surface

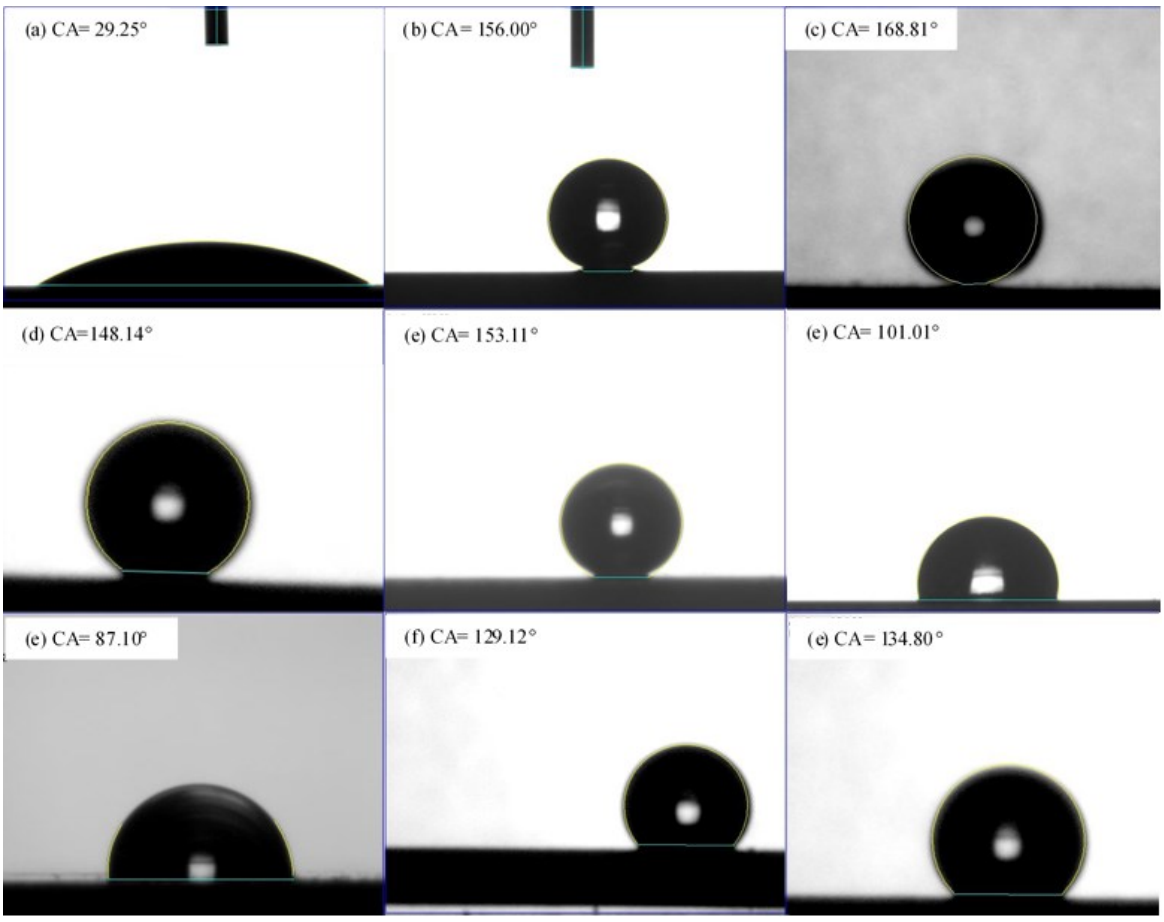

Figure-13 Contact angle measurements of superhydrophobic surfaces at different stages: (a) a cleaned bare TNA surface, TNA surface functionalized by (b) ODPA and (c) PFDPA molecules, respectively, (d) ODPA and (e) PFDPA functionalized TNA surfaces after 60 minute of ultrasound, (f) PFDPA and (g) ODPA functionalized surface after 70 minutes of ultrasound, with superhydrophobicity lost; (h) ODPA and (9)PFDPA functionalized surface after being placed in ambient overnight.

(figure 13(f)) and 133±2° for PFDPA coated surface (figure 13(g)). This is the first time that the recovery of superhydrophobic properties has been observed. Additionally, the wear resistance and contact angle recovery of the superhydrophobic property of these functionalized TNA surfaces has also been tested under a water jet before and after perturbation.

3.4 Conclusion

In conclusion, the Cassie-Baxter state, which corresponds to non-sticky superhydrophobic surfaces, has been successfully achieved by using long carbon chain molecules as self-assembled monolayers, passivating the TNAs surface. At the same time, the strong affinity of the phosphonate group to chemically bond with metal oxides has been temporarily inhibited by subjecting the surface with high intensity ultrasound energy. Observation has shown that both OPDA and PFDPA functionalized surfaces have survived 60 minutes of 225 Watts of ultrasound but will break down after 10 more minutes (70 minute total) of sonication. An interesting phenomenon observed is that the static contact angle recovers when the disrupted sample was placed overnight in an ambient environment. FTIR measurements have confirmed that the organic molecules stayed intact the whole time, which enables the eventual recovery of hydrophobicity. The strong bonding between phosphonic head groups with the TNA surface is worth noticing, as such knowledge about bonding response to kinetic energy is rarely seen. In addition, the industrial value of the passivated TNAs should not be neglected as the TiO_2 is naturally a ceramic and chemically inert to most of acids and bases. Further exploration is expected to be done to test its stability under ultrasound in solution with different PH values.

Chapter 4. TNA-Based Anti-Fouling Superhydrophobic Surface

4.1 Introduction of TNA-Based Anti-Fouling Superhydrophobic Surface

Fouling is one of the most significant concern in a lot of industries. There are many kinds of fouling, among all the scaling of water or "crystallization fouling" [64] is the most common in industry. The concept is simple, the minerals in water: usually Calcium, Magnesium, and Sodium salts precipitate onto the surfaces of containers, pipelines, and other possible equipment in a plant. The scale will accumulate and decrease the flow rate in pipelines; as an example a heat-exchanger, scaling will cause imbalance in heat change due to the reduction in flow rate as well as heat conduction, which then will cost more energy input to reach the targeted temperature, or more energy for replacing parts. A similar issue is in boilers, where condensation of steam will cause scaling, when the scale accumulate, the heat transfer rate is decreased between chamber walls, which will decrease the efficiency of the boiler. Current industrial treatments including chemical wash and physical abrasion (sand blasting, water jetting) are not very effective but very costly[65].

Utilizing the advantage of low surface energy of superhydrophobic TNAs surface, it is believed that the superhydrophobic TNAs are a good candidate for anti-fouling surfaces. The scale is not likely to form on the superhydrophobic surface because the low surface energy prevents nucleation from occurring.

4.2 The Anti-Fouling Test

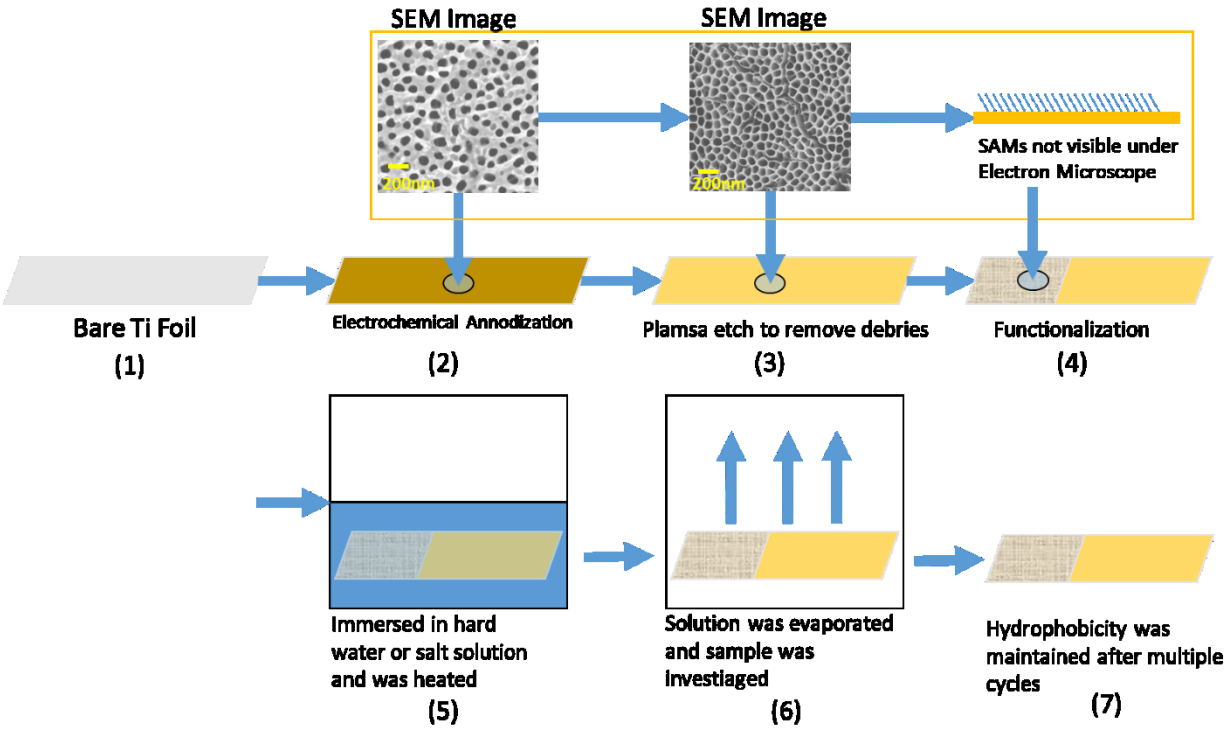

Figure 14: Process flow of making the superhydrophobic TNAs (1-4) and the anti-fouling test (5-7).

A simple yet effective test was chosen to test the anti-fouling. As illustrated in figure 14, the as-fabricated TNA sample is partially functionalized to be superhydrophobic, the sample was placed in glassware that is partially filled with hard water and later with salt water, which was then heated to about 100°C on a hot plate. Note that the sample was only partially functionalized with half of the sample SAMs free for comparison. As the liquid evaporates, the minerals in hard water or the salt in salt water (equal molar solution of 0.1 moles of $MgCl_2$ and $NaCl_2$) will precipitate. The process is repeated multiple times without removing the TNA sample, which is meant to simulate a common environment in a heat exchanger or a boiler. The result can be distinguished with visual inspection as well as energy dispersion x-ray spectroscopy (EDX).

4.3 Results and Discussion

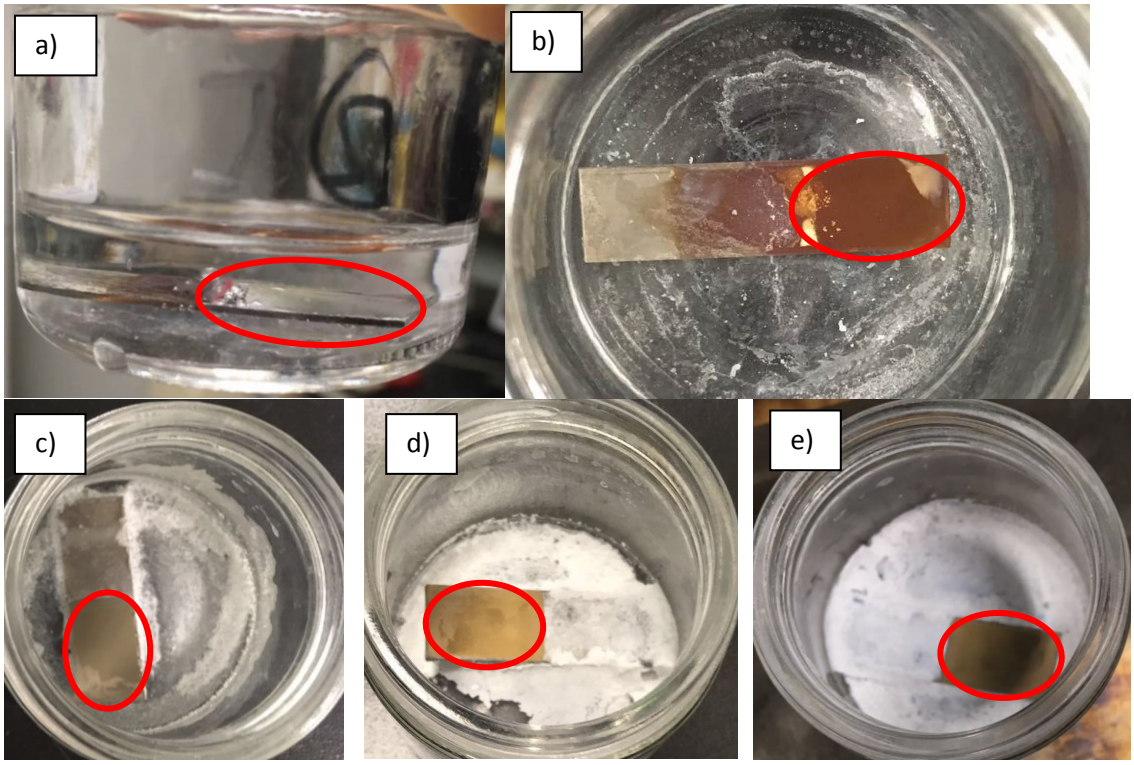

Figure 15: (a) The sample of half functionalized TNAs surface in water, red circle shows air gap between surface and water. (b) After the liquid is evaporated, red circle shows functionalized surface, (c) with salt water, after the liquid evaporated, (d) after the test repeat for three times (e) Five times.

Visual observations were performed throughout the test. From the start of step 5 stated in figure 14, when the sample was immersed in the glassware, the functionalized part of the sample turned a silver color immediately (red circled in Figure 15(a)). This is a sign of superhydrophobicity, where there is thin layer of air between the surface and water since water is not wetting the surface. When water is fully evaporated (figure 15(b)), the functionalized part was visually scale free and with rest of the sample cover in scale. The same results were obtained after multiple cycles. In figure 15(c),(d), and (e), the same evaporation test was done using salt, for 1 times, 3 times, and 5 times, respectively (without cleaning the glass or taking out the samples, only refilling the liquid after each cycle). As shown in the images, the functionalized part is salt free.

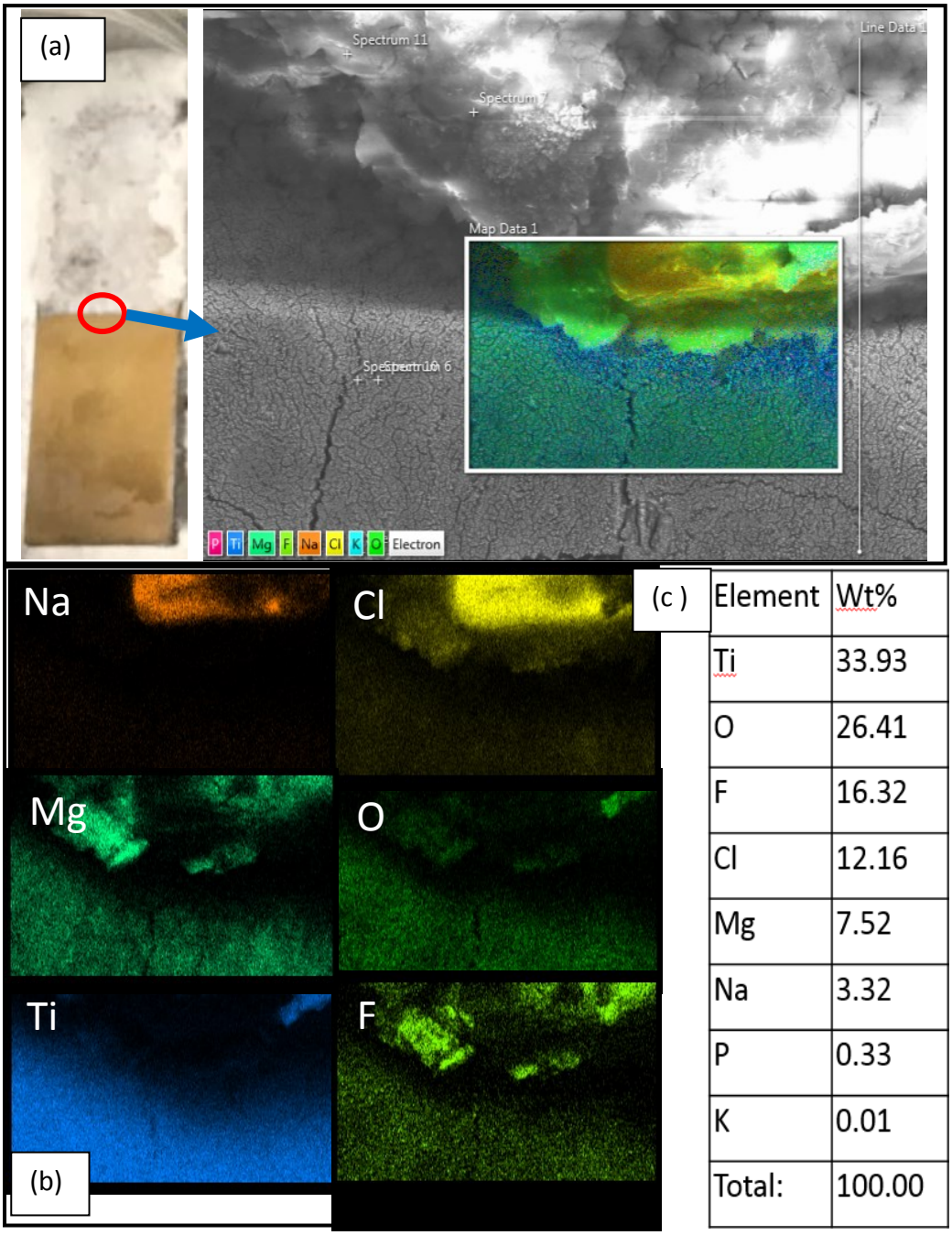

Element	Wt%
Ti	33.93
O	26.41
F	16.32
Cl	12.16
Mg	7.52
Na	3.32
P	0.33
K	0.01
Total:	100.00

Figure 16: (a) photograph (left) and SEM image with EDX map scan marked (right) of the partially functionalized TNAs. (b) Maps of single elements. (c)List of the elements and weight percentage.

To further verify if the functionalized surface is scale free: after 5 cycles of evaporation test with salt water, the sample was investigated with SEM and EDX. As shown in figure 16 (a) an image of the sample as well as a SEM image showing the selected area of the sample. The border of the

salt covered surface and the functionalized surface shows the transition from a salt covered and a salt free surface. An EDX element map scan was performed at the tip of the edge of the two area, the area is framed and decorated with color that represents elements. In part (b), six individual maps for single element is shown. It is clear that the crystal part is the Na and Mg salt in the solution, as most Na, Mg, and Cl elements are located in that area. The Ti and O element maps tells that the rest of the surface are TNAs. The fluorine mainly comes from the SAM molecule PFDPA, it appears not only in the TNAs area, which might be due to the diffusion of the physisorbed molecules. Similar phenomenon is also observed with Mg, where on TNAs surface there is Mg signal. Part (c) is list of elements that show up in the map scan and their wt%.

4.4 Conclusion

The anti-fouling ability of the superhydrophobic TNAs is tested using an evaporation test by placing samples into glassware that heat up to evaporate the solution, which is meant to simulate an industrial setup. On both hard water and salt water, there is no visual evidence of crystallization or scale at the functionalized superhydrophobic surface. EDX mapping result also confirmed that on a microscale, a distinguishable difference can be observed at the SAM functionalized to SAM free border.

Chapter 5. Transparent TiO_2 Nanowire Arrays (TNWs) Superhydrophobic Surface

5.1 Introduction to TNWs Superhydrophobic Surface

Transparency is a very important parameter for optical equipment and devices (*e.g.* windows, lenses and solar panels). Over the last few decades, enormous research effort has been devoted to protecting these transparent surfaces from microbial growth, ice formation, corrosion, and fouling due to long term exposure in different harsh environmental conditions. In the literature, numerous fabrication techniques have been reported which are typically focused on growing well-defined rough structures on different surfaces in order to make a superhydrophobic surface [66-69]. On the other hand, surface roughness leads to opacity due to undesired light scattering. Light scattering probability is determined by the roughness solid fraction of the surface and the refractive index of the materials [70]. The contact angle increases with roughness of the hydrophobic surface at a certain limit; meanwhile, the transparency decreases with the roughness due to the scattering of light from the rough surface. Therefore, the main challenge is to control the roughness size scale as well as the refractive index of the coating materials on the substrate, in such a way as to substantially decrease the light scattering probability and achieve a highly transparent superhydrophobic surface. It is worth mentioning that simultaneously achieving highly transparent and superhydrophobic surfaces typically requires $\leq$ 100 nm feature sizes on the surface. Fabrication of transparent superhydrophobic surfaces using plasma etching was first demonstrated by Ogawa et al. [71]. Engineering of transparent superhydrophobic surfaces by a grid pattern technique was also reported [72]. Recently, a simple and cost effective way of

making highly transparent and superhydrophobic surfaces using 3-aminopropyltrimethoxysilane (APTS)-functionalized silica nanoparticles was demonstrated by Karunakaran et al. [73]. Naoyuki et al. investigated the durability of transparent superhydrophobic surfaces [74]. K. Takai et al. also successfully prepared transparent superhydrophobic surfaces by coating TiO_2 thin films and subsequently passivating them with (fluoroalkyl) silane [75]. Herein, we describe a simple and versatile strategy to engineer transparent superhydrophobic surfaces via the hydrothermal growth of TNWs assembled on a fluorine-doped tin oxide (FTO) coated glass surface followed by coating the surface with long chain organic molecules, namely PFDPA. Initially, the TNWs were made hydrothermally on the FTO side of the FTO/glass substrate. Then the surface of TNWs was decorated with the PFDPA monolayer. The transparency has been measured by ultraviolet–visible (UV-Vis) spectrophotometry, which ≥ 80% transparency has been found in the visible spectral range. Moreover, the superhydrophobicity has been justified via CA measurement.

5.2 Preparation Procedure of Transparent Superhydrophobic TNWs

Fluorine-doped tin oxide (FTO) coated glass slide having a sheet resistance of 8 Ω/cm^2 was cleaned by sonicating it sequentially in acetone, methanol and deionized (DI) water. Rutile TiO_2 nanowire array was grown on cleaned FTO by simple hydrothermal method. 2.5 ml of hydrochloric acid (37%) and 2.5 ml of glacial acetic acid were mixed with 5 ml of DI water in ambient conditions. The mixture was transferred to a Teflon lined stainless steel autoclave after adding 600 µl of titanium butoxide. Pre-cleaned FTO substrate was placed in the autoclave tilted at an angle such that the nonconductive side faced upwards and the conductive side faced

downwards. The autoclave was then properly sealed and hydrothermal growth was conducted at 200 ºC for 30 min in a gravity convection oven. Subsequently, the autoclave was cooled to room temperature naturally, and the resulting transparent nanowire array was then rinsed properly with DI water and dried by nitrogen gas flow.

The cleaned TNW array was then immersed in 1mM PFDPA (purchased from Aculon) solution in methanol (99.8% purity) at room temperature for 18 to 20 hours in order to functionalize the surface by forming a self-assembled monolayer of PFDPA on TiO_2. Afterwards, the modified surface was rinsed with methanol properly to remove all physisorbed molecules and dried thoroughly with N_2 gas flow.

5.3 Results and Discussion

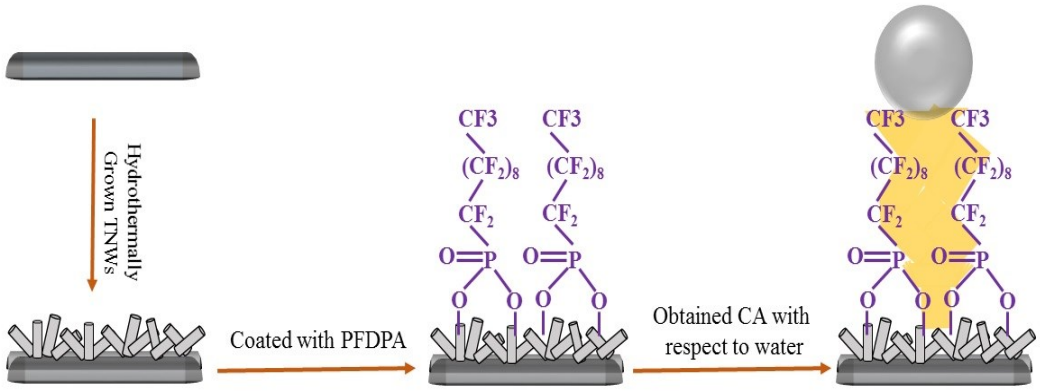

Figure 17: Schematic representation of the making of transparent superhydrophobic surfaces

Figure 17 illustrates the process of making the transparent functionalized TNW surface, utilizing hydrothermally grown TNWs followed by functionalization. It is well documented that the phosphonate group has a high propensity to make a strong bond with metal oxides and this property has been exploited in our case. The nanostructures of metal oxides such as TiO_2 are superior to a

flat TiO_2 surface because they minimize the fraction parameter of the contact area with water. This results in an easily achieved higher static contact angle [35, 59, 60], pertaining to a Cassie-Baxter state (79) due to trapped air states inside the micro/nano structure. The dimension and texture of the TNWs has been measured using field emission scanning electron microscope (FE-SEM) (ZEISS SIGMA field emission electron microscope).

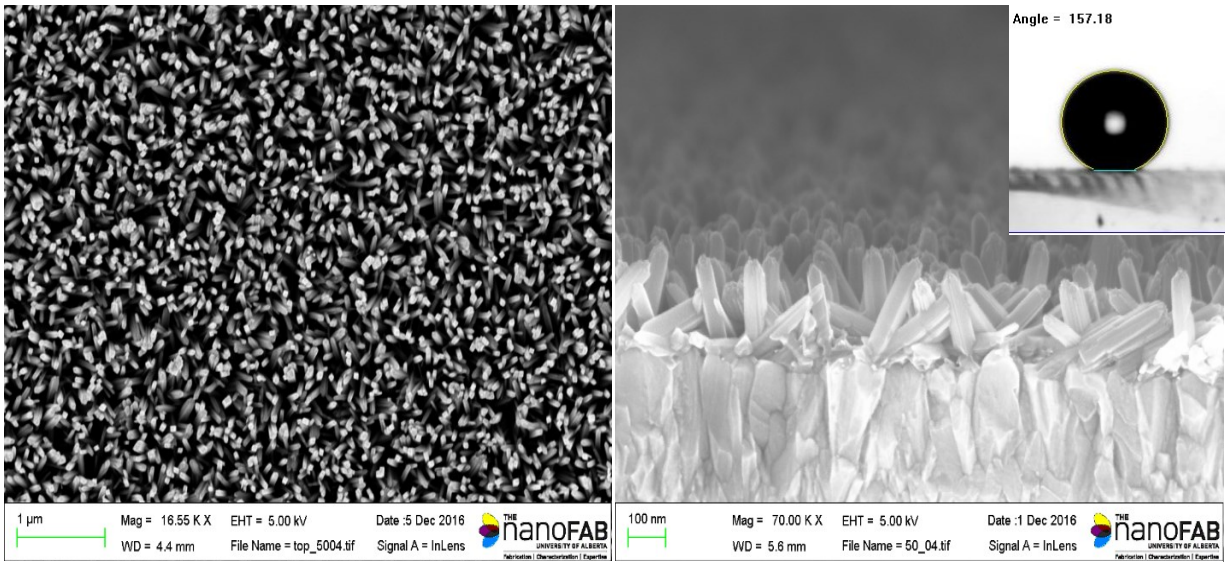

Figure 18: The top view of the TNWs array. (b) The side view of the TNWs array, shows the random orientation of the TNWs. Inset: The contact angle of the transparent sample, showing a 157.18° contact angle.

Figure 18 depicts the FE-SEM images of the nanostructures, which reveal that the length of individual nanowire is in the range of 100 to 200 nm and the radius is approximately 30 nm. Interestingly, figure 18 (b) shows that the TNWs have grown chaotically on the surface. Presumably, this random orientation of the TNWs on the surface will provide the adequate roughness and hierarchy, which will help to create enough air trap states such that they exhibit anti-wetting properties immediately after the conformal coating with organic molecules. The superhydrophobic properties have been confirmed by investigating the contact angle (by a FTA-200 system) of the functionalized TNW surface with PFDPA molecules and it was found that the contact angle with respect to a 4 µl water droplet is $> 150^0$ (Fig. 19). In contrast, the unpassivated

transparent TNWs exhibited $<10^0$ CA with an equal volume water droplet and this value is in good agreement with literature [76]. Moreover, the wear resistance of the surface has been corroborated

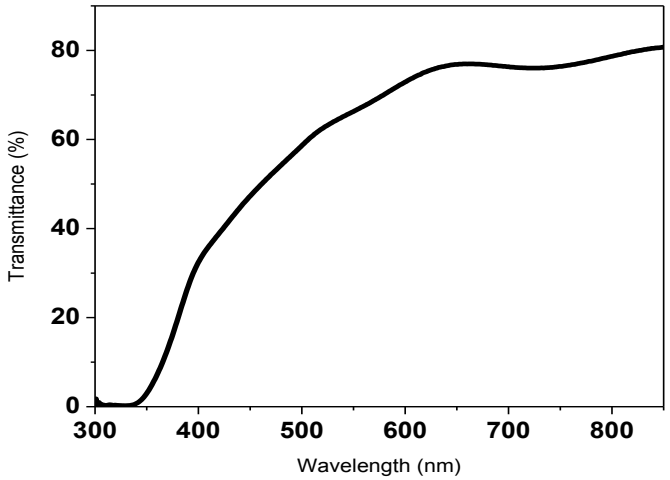

Figure 19: The UV-Vis spectra of the PFDPA coated TiO_2 nanowire array on FTO glass.

by applying a water jet on the surface.

The transparency of the PFDPA coated TNW surface was monitored by UV-Vis measurements. Figure 19 shows that at wavelengths higher than 600 nm, a transmittance of about 80 % is observed, which then drops to about 60 % at a wavelength of 500 nm. A significant decrease in transmittance to approximately 35 % is observed at the wavelength of 400 nm which is close to the TiO_2 bandgap (390 nm).

5.4 Conclusion

A superhydrophobic and transparent surface is obtained by synthesizing TiO_2 nanowire arrays on FTO glass, followed by functionalization with PFDPA molecules. The contact angle observed is about 157° which clearly suggests that the surface becomes superhydrophobic. The UV-Vis spectra show that the surface is transparent. The hallmark of this process is that this is a very simple route of synthesis for engineering a transparent superhydrophobic surface. Most importantly, the

random orientation of the nanowires is ideal for the surface in order to replicate the “lotus effect” seen in nature. In the future, it is possible to control the transparency of the film within the visible spectrum by optimizing the aspect ratio and Mie scattering properties of the nanowires.

Chapter 6. Superhydrophobic Coating Based On TiO_2 Nanoparticles (NPs) and Polydimethylsiloxane (PDMS)

6.1 Introduction to coating based on TiO_2 NPs and PDMS

As previously mentioned, a suspension made from nanoparticles and PDMS can be sprayed as a superhydrophobic coating. TiO_2 NPs are one of the great candidates to make such a coating due to their properties such as photoreactivity and mechanical durability. After being mixed with PDMS and suspended in an organic solution, the mixture can be sprayed onto almost all substrates, benefitting from PDMS's great adhering property. The most remarkable property of this film is that the spray technique does not require expensive equipment due to which it has high scalability when it comes to industrial application. According to previous reports, the TiO_2-PDMS mixture has been proven to be self-recoverable and repairable [77, 78], which makes the coating resistant to permanent damage.

6.2 Preparation Procedure

6.2.1 Materials

Degussa P25 TiO_2 nanoparticles (NPs) and tetrahydrofuran (THF) are obtained from Aldrich. SYLGARD® 184 silicone elastomer kit is obtained from Dow Corning and 2.5 cm square glass slides are obtained from Fisher Scientific.

6.2.2 Suspension Preparation and coating procedure

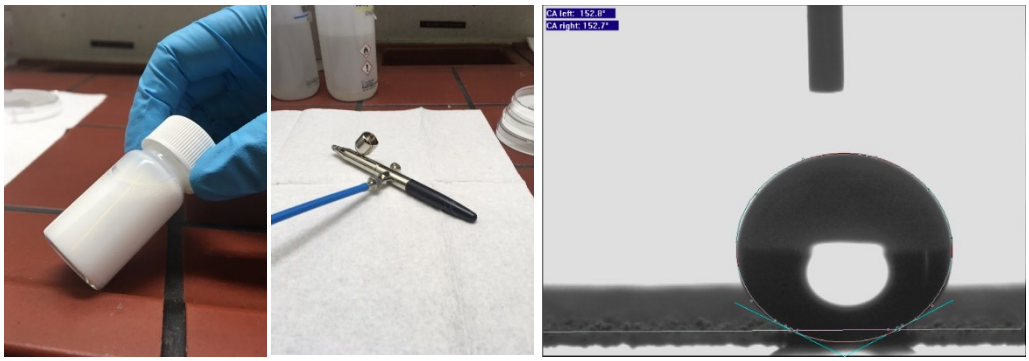

Figure 20: Image of (a) the suspension of TiO_2-PDMS. (b) The triplex II air brush. (c) The contact angle of the obtained film, with a droplet of 10 µL of DI water.

In a typical experiment, the TiO_2 NPs are suspended in THF, at around 4 wt%, and PDMS was subsequently added to the suspension at a 1:1, 2:1 or 3:1 weight ratio to TiO_2. The suspension is then sonicated in a horn sonicator from Branson. The obtained turbid suspension (Figure 20 (a)) is then mixed with a curing agent. Thereafter, the mixture is loaded into the funnel of a Triplex II air brush from Gabbert Airbrushtechnik (Figure 20 (b)). The square glass slide is taped on a hotplate that is pre-heated to 70 °C. The suspension is sprayed onto the glass substrate right away after loading. Spray distance is around 15 to 20 cm from the substrate and a zig-zag hand motion is maintained through the spraying process. Once the spray has covered the substrate with three layers, the sample is moved to another hot plate at 150 °C for fast curing.

6.3 Results and Discussion

6.3.1 Morphology of the coating

The obtained film shows superhydrophobicity as shown in figure 20(c). To understand the underlying reason of why the mixture coating can simply provide a hydrophobic surface, both light microscope (LM) and SEM image were taken to investigate the coating's micro- and nano-

structure. Figure 21 includes both a LM image (a) and few SEM images ((b)(c)(d)) of a typical sample. The formation from (a) to (d) is meant to show the micro-nano dual structure that forms naturally when the mixture is sprayed as a coating. This dual structure is known to be the key to the so called “lotus effect”, where similar structures were first found in lotus leaves (1). In this case, the agglomeration of TiO_2 NPs is covered with a thin layer of PDMS, which is ideally thin enough so that the rough feature of TiO_2 NP agglomeration is not buried while not exposing the TiO_2 NPs to the surface since they are hydrophilic. The superhydrophobicity shown by the

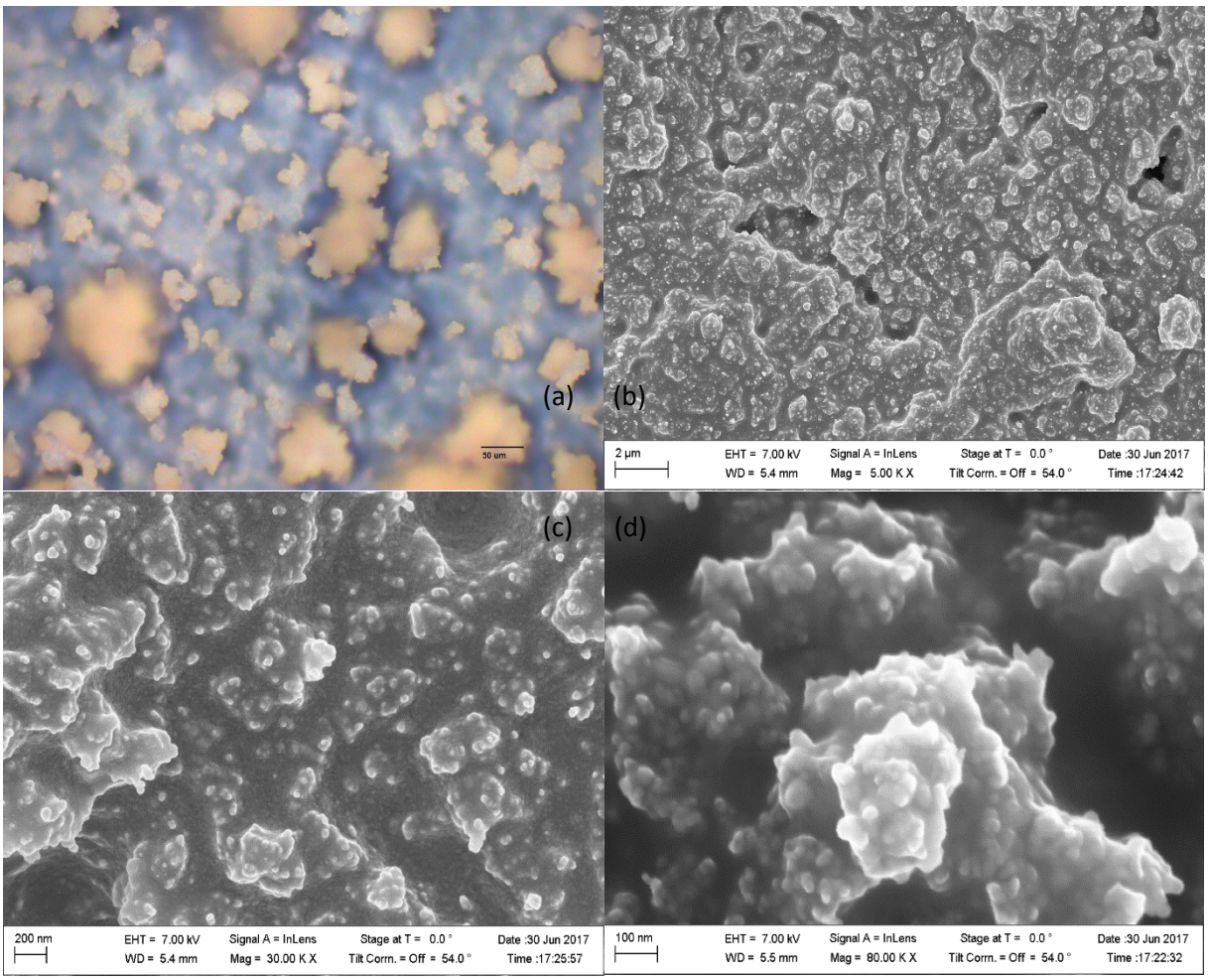

Figure 21: LM ((a)) and SEM ((b), (c), (d)) images showing the micro- and nano-structures of the coating. 2(a), Micro-sized features that looks like rocks, which scattered everywhere; these are actually agglomerations of TiO_2 nanoparticles sealed in PDMS. 2(b), 2(c) and 2(d) shown a “zoomed-in” view from 5000 times magnification to 80,000 times. It can be clearly seen that the nano-sized features exist on the micro-sized features.

samples is a good example of the PDMS successfully covering the TiO_2.

6.3.2 Study of Fabrication Optimization

The mixture content of this sample is 4 wt % TiO_2 NPs and 5 wt % PDMS. Increasing the concentration of PDMS will eventually cause encapsulation of the rough features that are created by TiO_2 during curing, leading to a reduction in hydrophobicity.

To obtain a mixture that does not agglomerate such that it clogs the air-brush, a few solvents are tested, such as ethanol, isopropanol, methanol, n-hexane, and THF. Among all, THF has the best solubility of PDMS [79], which prevents clogging of the air-brush that occurs when PDMS is not well-dissolved and starts to polymerize at the nozzle. It also provides a "dry" spray thanks to its high vapor pressure.

6.3.3 Robustness of the sprayed film

PDMS is hardened after curing, which results in a robust film which sticks to the surface tightly. Rubbing the film with fingers in nitrile gloves hardly removes any material. An abrasion test is also done, following the ASTM standard D968-17. In this test, 2L of silica sand falls on the sample surface from a funnel that is at the top of a 36'' (91.4cm) tube that has a 0.75'' (1.9cm) inner diameter. 3D maps from a Bruker Dektak XT profilometer and LM image are taken before and after abrasion test, as shown in figure 22, In order to test the limit of the sample, the test is carried out by adding up the sand volume to 5 L instead of 2 L in the standard procedure. As seen in the 3D map and the LM image, the abrasion causes the features to reduce to a finer, smoother topography (i.e, rough features on the surface are reduced in thickness and size)

Meanwhile, it is safe to say that the roughness of the surface is maintained in this way. The contact angle test is performed and as expected, the superhydrophobicity is not disrupted by abrasion (CAs are shown in insets). Other tests related to robustness are to be performed in the future as well, such as subjecting the sample to oxygen plasma, ultra-violet (UV) illumination, and varying temperature and humidity (climate chamber), to provide more insights regarding the robustness of the film.

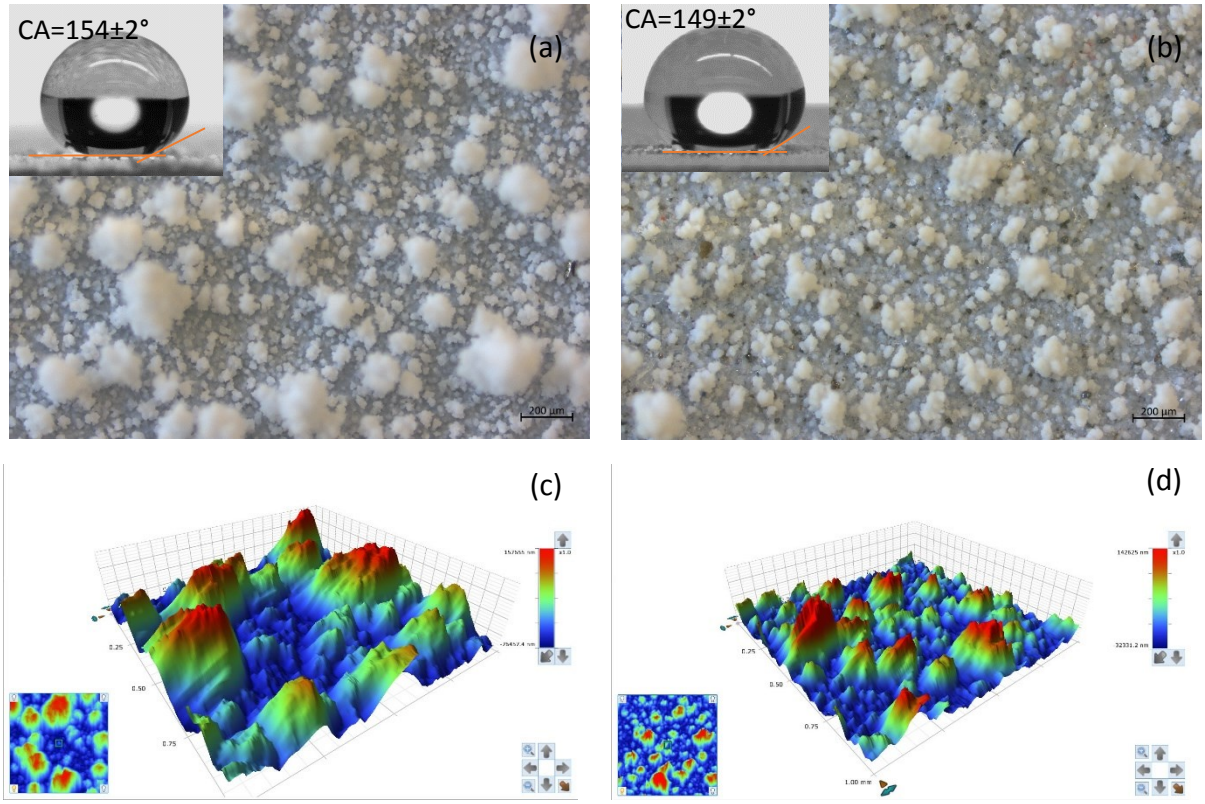

Figure 22: (a) and (b) LM image the before and after 5 L of sand abraded coating.(c) and (d), the 3D depth map of before and after abraded coating. Insets: The photograph for CA measurement for (a) and (b).

6.4 Conclusion

A TiO_2 NP and PDMS based superhydrophobic coating is obtained. It is shown that the coating has a micro-nano dual structure that is naturally formed during the drying process. According to the predictions of the theory, this structure allows the coating to exhibit a Cassie-Baxter state, leading to hydrophobicity. A cured PDMS-TiO_2 NP mixture also exhibits robust mechanical properties as indicated by the fact that it survived the coating integrity test based on an ASTM standard, namely the sand abrasion test. In the future, it will be beneficial if the coating system can be further explored by expanding it to coatings made from other nanoparticles combined with PDMS. This is very possible because the superhydrophobicity of the coating is naturally formed during the drying process, as long as the two materials are half-miscible to allow the PDMS coverage without completely encapsulating the rough features. Ideally, each successful system with different nanoparticles should benefit from the nanoparticle properties combined with superhydrophobicity. Finally, the PDMS can be changed to other polymers to improve certain properties such as mechanically durability or incorporate other properties as needed. Overall, this work has demonstrated a simple way to utilize TiO_2 NPs in preparing a robust superhydrophobic coating, which should open doors to other possible systems.

Chapter 7. Electrowetting on Functionalized Nanowire & Nanotube Surfaces

7.1 Introduction of EWOD on Superhydrophobic TNAs and TNWs

Based on the EWOD theory, one can build an EWOD system based on superhydrophobic TNWs or TNAs. TNWs usually grown on conductive substrates such as FTO coated glass or Ti foils or highly doped silicon wafers, which matches with the structure of an EWOD device where a hydrophobic and dielectric layer are built on top of a conductive substrate. A similar idea can be applied to TNAs as well. Figure 23 shows the photographs of TNW and TNA EWOD setups ((a) and (b)) and a schematic of the setup(c). The advantage of using TNWs or TNAs to build EWOD devices is that there is no need for extensive vacuum deposition or polymerization of a very thin polymer dielectric layer; as the nanostructure is grown at the substrate from simple chemical/electrochemical process, namely, hydrothermal synthesis (TNWs) and anodization (TNAs). The thickness of the dielectric layer can also be changed simply by varying the synthesis conditions. In addition to benefiting from the wide application of hydrothermal and anodization processes, the system can also be expanded to include other metal oxide dielectric nanostructures.

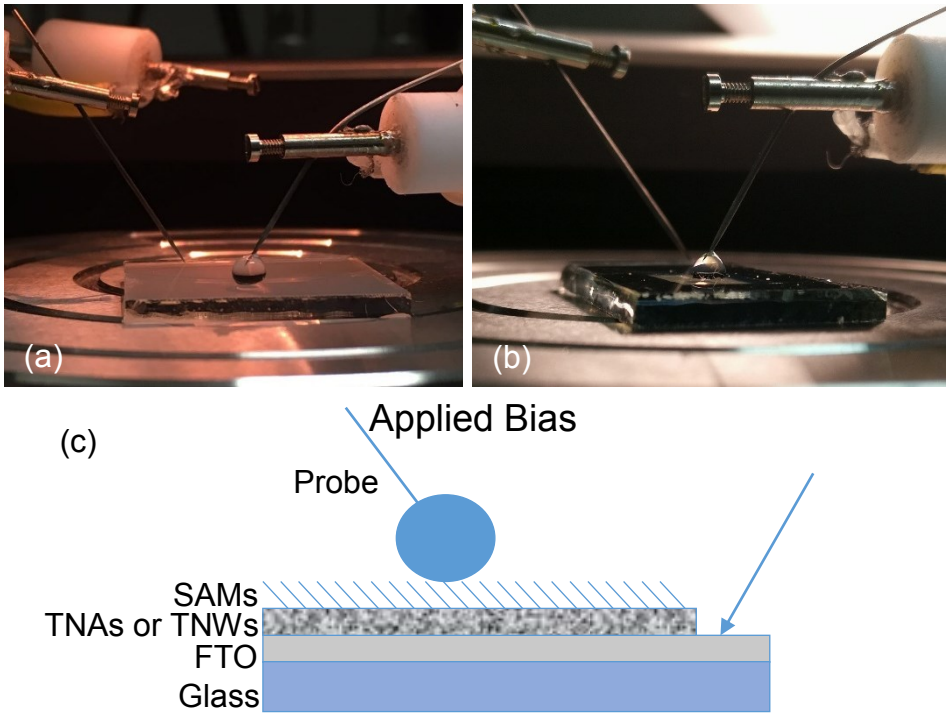

Figure 23: Photographs of TNWs (a) and TNAs (b) setup. (c) Scheme of the TNAs or TNWs EWOD setup.

7.2 Preparation of the EWOD Setup of Superhydrophobic TNAs and TNWs

The superhydrophobic TNAs and TNWs are prepared as mentioned previously. When the samples are ready, the sample is placed on the stage of a Keithley 4200 probe station. As shown in figure 23, a droplet of 5 µL DI water (or salt water, depends on experiment interest) is placed between one of the steel measuring probes and the superhydrophobic surface. To complete the circuit, another probe is placed directly on top of the FTO conducting layer. A bias is then applied on the probe that is connecting the droplet. Then, the response of the droplet (change in contact angle and shape) is recorded by a camera.

7.3 Results and Discussion

Figure 24 is a set of images that show the decrease in contact angle on a superhydrophobic TNAs surface when a positive voltage is applied at the probe over a period of time. In this case, applied

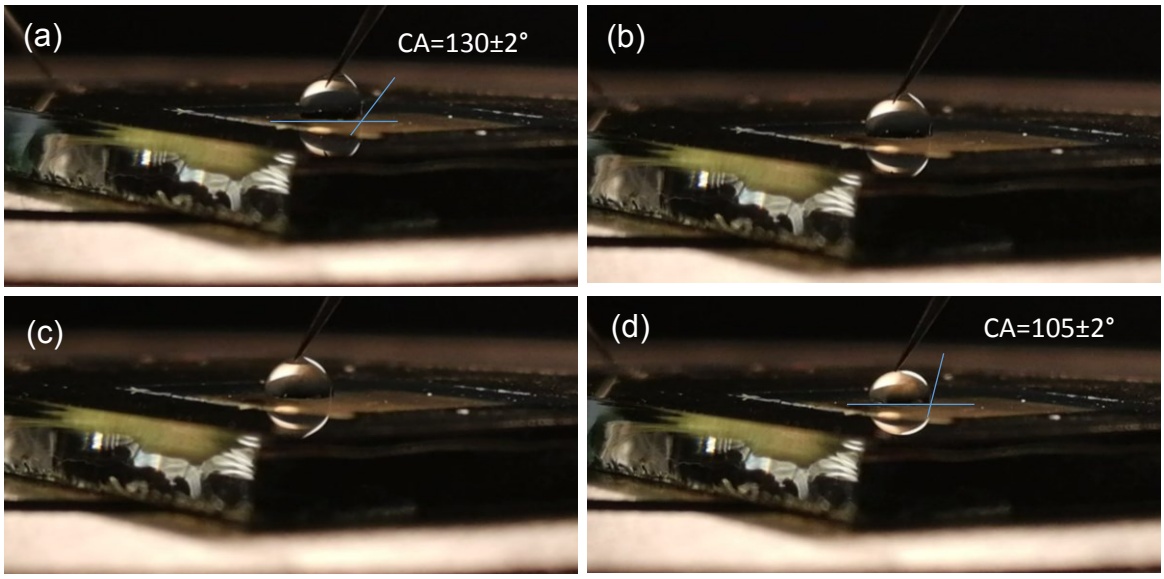

Figure 24:Images of response of a droplet on superhydrophobic TNAs surface when applied constant bias as time ellipse.(a) Starting off,(b) 60s (c) 150s (d) 240s.

until the droplet is "pushed" to the surface so there is no electric connection. The TNA thickness is approximately 1 μm and in this specific experiment, the applied voltage is 2 V. According to Wyatt et al., much higher voltage (50 V, 200 V, etc) have been used in EWOD in the past when the dielectric layer is thinner; the TiO_2 layer is thick considering as a dielectric layer in a EWOD device yet the actuation voltage is as small as 2 V. Unfortunately, there is still no clear explanation of this phenomenon yet, but it is possible that the TNAs surface is not as resistive as it seems, let alone the potential conduction in the SAM above the dielectric layer. Another possibility is that some water molecule at the top (connection to the probe) evaporates from time to time, as the changing contact angle is not as much as it appears to be. By looking closely to figure 24 (a) and (d), the difference in contact angle is about 25 degrees.

On the other side, a more obvious change in contact angle is seen in the superhydrophobic TNW surface, as shown in figure 25. The droplet on the left (10 µL) has been subjected to a 2 V bias over a time period of 720 seconds and when the probe is removed, the droplet stays on the surface. For comparison, another droplet (same volume) is placed at the surface without being subjected to any electrical bias. There is a clear change in contact angle, a difference of 36 degrees, as measured.

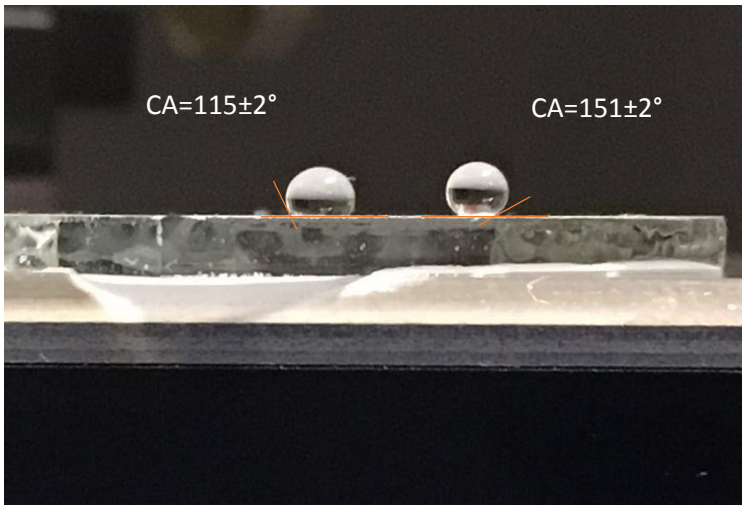

Figure 25: Two water droplets standing on the TNW superhydrophobic surface. The droplet at left has been subjected to a bias while the droplet on the right is not.

7.4 Conclusion

EWOD devices are successfully fabricated on both TNA and TNW superhydrophobic surfaces. Though the response time is slow, comparing to the state-of-art setups (few hundred seconds to within a second), there is clearly potential in building EWOD devices based the TNAs and TNWs thanks to their simple and low cost fabrication methods. For example, if the thickness can be brought down to within 100 nm, the change in contact angle can be dramatically improved as predicted by the Lippman equation.

Chapter 8. Summary

The work of this Masters Thesis on superhydrophobic surfaces is highly applicable to commercial industry. Benefiting from their nanoscale structures, hydrophobic surfaces constructed from TNAs and TNWs can be used in many scenarios. The most remarkable advantage of these nanostructures is they are all formed from self-organizing chemical processes, i.e., they are all bottom-up processes where no lithography or extensive vacuum deposition is needed. Moreover, by simply varying experimental conditions, one is able to precisely (to 10s of nm) manipulate certain properties (length and width of features, packing, and crystallinity). These processes are also adaptable to many other non-native surfaces, which enables more substrates for fabrication so that more research interests can be explored.

As demonstrated in this thesis, the manipulation of properties leads to robust surfaces. For example, the ultrasound and the fouling experiments mentioned in Chapters 3 and 4 have proven that the TNAs are resistant to harsh environmental conditions. Similarly, the sand abrasion test mentioned in Chapter 6 has proven that the TiO_2-PDMS coating is mechanically robust. Additionally, transparent and superhydrophobic surfaces can be obtained by manipulating the dimensions of TNWs as mentioned in Chapter 5. All these results benefit from the highly controllable experimental processes which lead to precisely controlled shapes and dimensions in the final products.

In addition to the above mentioned applications of superhydrophobic surfaces, the surface itself is a good platform to perform other experiments on, and the EWOD devices mentioned in Chapter 7 provide a good example of this. The significance of the superhydrophobic surfaces

prepared and studied in this thesis also derives from the fact that TiO_2 is also a well-known material for solar cell and photocatalytic applications. The bio-compatibility of TiO_2 also gives rise to research interest in implants and drug delivery.

Overall, the TiO_2 based nanostructures are a great candidate to fabricate robust super-hydrophobic surfaces. The process of fabricating such a surface is simple and cost effective. The application potential is high thanks to the great properties of TiO_2 itself. Meanwhile, the TiO_2 superhydrophobic surfaces are great platforms for other research interests as well. In the future, the superhydrophobic surfaces can be enhanced even further to be able to compete with commercial products and a lot of other systems based on similar principles can be researched; thus such surfaces can be fabricated with different materials, and designed to benefit from their respective properties.

Biliography

[1] W. Barthlott and C. Neinhuis, "Purity of the sacred lotus, or escape from contamination in biological surfaces," *Planta,* journal article vol. 202, no. 1, pp. 1-8, April 01 1997.

[2] S. Banerjee, "Simple derivation of Young, Wenzel and Cassie-Baxter equations and its interpretations.," *cond-mat.soft,* vol. 08, no. 08, 2008, Art. no. 1460.

[3] R. N. Wenzel, "Resistance of solid surfaces to wetting by water," *Industrial & Engineering Chemistry,* vol. 28, no. 8, pp. 988-994, 1936/08/01 1936.

[4] A. B. D. Cassie and S. Baxter, "Wettability of porous surfaces," *Transactions of the Faraday Society,* 10.1039/TF9444000546 vol. 40, no. 0, pp. 546-551, 1944.

[5] H. Teisala, M. Tuominen, and J. Kuusipalo, "Superhydrophobic Coatings on Cellulose-Based Materials: Fabrication, Properties, and Applications," *Advanced Materials Interfaces,* vol. 1, no. 1, pp. 1300026-n/a, 2014, Art. no. 1300026.

[6] Z. Guo, W. Liu, and B.-L. Su, "Superhydrophobic surfaces: From natural to biomimetic to functional," *Journal of Colloid and Interface Science,* vol. 353, no. 2, pp. 335-355, 2011/01/15/ 2011.

[7] A. del Campo and E. Arzt, "Fabrication Approaches for Generating Complex Micro- and Nanopatterns on Polymeric Surfaces," *Chemical Reviews,* vol. 108, no. 3, pp. 911-945, 2008/03/01 2008.

[8] T. Darmanin, E. T. de Givenchy, S. Amigoni, and F. Guittard, "Superhydrophobic Surfaces by Electrochemical Processes," *Advanced Materials,* vol. 25, no. 10, pp. 1378-1394, 2013.

[9] X. Wang, B. Ding, J. Yu, and M. Wang, "Engineering biomimetic superhydrophobic surfaces of electrospun nanomaterials," *Nano Today,* vol. 6, no. 5, pp. 510-530, 2011/10/01/ 2011.

[10] M. Liu, Y. Zheng, J. Zhai, and L. Jiang, "Bioinspired Super-antiwetting Interfaces with Special Liquid−Solid Adhesion," *Accounts of Chemical Research,* vol. 43, no. 3, pp. 368-377, 2010/03/16 2010.

[11] B. Bhushan, "Biomimetics inspired surfaces for drag reduction and oleophobicity/philicity," *Beilstein Journal of Nanotechnology,* vol. 2, pp. 66-84, 02/01

[12] M. Qu, J. He, and J. Zhang, "Superhydrophobicity, Learn from the Lotus Leaf," in *Biomimetics Learning from Nature*, A. Mukherjee, Ed. Rijeka: InTech, 2010, p. Ch. 16.

[13] "Summary and conclusions of the sixty-seventh meeting of the Joint FAO/WHO Expert Committee on Food Additives," in *Joint FAO/WHO Expert Committee on Food Additives*, Rome, Italy, 2006, no. 7: FAO/WHO.

[14] C. Steinbach. (2016, dec21). *Nanoparticles in paints*. Available: https://www.nanopartikel.info/en/nanoinfo/cross-cutting/2021-nanoparticles-in-paints#literatur

[15] (2017). *Titanium Dioxide; Exemption From the Requirement of a Tolerance*.

[16] R. P. P. G. Sheasby, "*The Surface Treatment and Finishing of Aluminium and Its Alloys*." ASM International, 2001.

[17] M. RHODES. (2016, DEC 20). "How apple made its jet black iphone none more black." Available: https://www.wired.com/2016/09/apple-jet-black-iphone-none-more-black/

[18] J. M. Macak, K. Sirotna, and P. Schmuki, "Self-organized porous titanium oxide prepared in Na2SO4/NaF electrolytes," *Electrochimica Acta,* vol. 50, no. 18, pp. 3679-3684, 2005/06/10/ 2005.

[19] H. Tsuchiya *et al.*, "Self-organized TiO2 nanotubes prepared in ammonium fluoride containing acetic acid electrolytes," *Electrochemistry Communications,* vol. 7, no. 6, pp. 576-580, 2005.

[20] J. M. Macak, H. Tsuchiya, L. Taveira, S. Aldabergerova, and P. Schmuki, "Smooth anodic TiO2 nanotubes," *Angewandte Chemie - International Edition,* vol. 44, no. 45, pp. 7463-7465, 2005.

[21] S. Nagai, "Hydrothermal Reactions for Materials Science and Engineering," *Elsevier Applied Science,* vol. 40, 1989.

[22] K. Byrappa and M. Yoshimura, "2 - History of Hydrothermal Technology," in *Handbook of Hydrothermal Technology (Second Edition)*Oxford: William Andrew Publishing, 2013, pp. 51-73.

[23] E. S. C. Friedel, *Compt. Rend.,* no. 92, p. 4, 1881.

[24] S. Meunier, "Production et cristallisation d'un silicate anhydre (enstatite) en presence de la vespeur d'eau a´ la pression ordinaire," *Compt. Rend.,* vol. 99, p. 2, 1880.

[25] E. Hosono, S. Fujihara, K. Kakiuchi, and H. Imai, "Growth of submicrometer-scale rectangular parallelepiped rutile TiO2 films in aqueous TiCl3 solutions under hydrothermal conditions," *Journal of the American Chemical Society,* vol. 126, no. 25, pp. 7790-7791, 2004.

[26] C.-C. Weng, K.-F. Hsu, and K.-H. Wei, "Synthesis of arrayed, TiO2 needlelike nanostructures via a polystyrene-block-poly (4-vinylpyridine) diblock copolymer template," *Chemistry of materials,* vol. 16, no. 21, pp. 4080-4086, 2004.

[27] K. Kakiuchi, E. Hosono, H. Imai, T. Kimura, and S. Fujihara, "{111}-faceting of low-temperature processed rutile TiO 2 rods," *Journal of crystal growth,* vol. 293, no. 2, pp. 541-545, 2006.

[28] X. Feng, J. Zhai, and L. Jiang, "The fabrication and switchable superhydrophobicity of TiO2 nanorod films," *Angewandte Chemie International Edition,* vol. 44, no. 32, pp. 5115-5118, 2005.

[29] B. Liu and E. S. Aydil, "Growth of oriented single-crystalline rutile TiO2 nanorods on transparent conducting substrates for dye-sensitized solar cells," *Journal of the American Chemical Society,* vol. 131, no. 11, pp. 3985-3990, 2009.

[30] A. Kumar, A. R. Madaria, and C. Zhou, "Growth of aligned single-crystalline rutile TiO2 nanowires on arbitrary substrates and their application in dye-sensitized solar cells," *The Journal of Physical Chemistry C,* vol. 114, no. 17, pp. 7787-7792, 2010.

[31] W. C. Bigelow, D. L. Pickett, and W. a. Zisman, "Oleophobic monolayers. Films Adsorbed From Solution In Non-Polar Liquids," *Journal of Colloid Science,* vol. 1, no. 6, pp. 513-538, 1946.

[32] a. Ulman, "Formation and Structure of Self-Assembled Monolayers," *Chemical Reviews,* vol. 96, no. 4, pp. 1533-1554, 1996.

[33] E. L. Hanson, J. Schwartz, B. Nickel, N. Koch, and M. F. Danisman, "Bonding Self-Assembled, Compact Organophosphonate Monolayers to the Native Oxide Surface of Silicon," *Journal of the American Chemical Society,* vol. 125, no. 51, pp. 16074-16080, 2003.

[34] L. B. Boinovich, A. M. Emelyanenko, V. K. Ivanov, and A. S. Pashinin, "Durable icephobic coating for stainless steel," *ACS Applied Materials and Interfaces,* vol. 5, no. 7, pp. 2549-2554, 2013.

[35] S. Farsinezhad *et al.*, "Amphiphobic surfaces from functionalized TiO 2 nanotube arrays," *Rsc Advances,* vol. 4, no. 63, pp. 33587-33598, 2014.

[36] R. Helmy and A. Y. Fadeev, "Self-assembled monolayers supported on TiO2: Comparison of C18H37SiX3 (X = H, Cl, OCH3), C18H37Si(CH3)2Cl, and C18H37PO(OH)2," *Langmuir,* vol. 18, no. 23, pp. 8924-8928, 2002.

[37] G. Hähner, R. Hofer, and I. Klingenfuss, "Order and orientation in self-assembled long chain alkanephosphate monolayers adsorbed on metal oxide surfaces," *Langmuir,* vol. 17, no. 22, pp. 7047-7052, 2001.

[38] B. J. Lee, Z. Zhang, S. Baek, S. Kim, D. Kim, and K. Yong, "Bio-inspired dewetted surfaces based on SiC/Si interlocked structures for enhanced-underwater stability and regenerative-drag reduction capability," *Scientific reports,* vol. 6, no. April, pp. 24653-24653, 2016.

[39] Y. Chen *et al.*, "Transparent superhydrophobic/superhydrophilic coatings for self-cleaning and anti-fogging," *Applied Physics Letters,* vol. 101, no. 3, pp. 7420-7426, 2012.

[40] A. Steele, I. Bayer, and E. Loth, "Inherently superoleophobic nanocomposite coatings by spray atomization," *Nano letters,* vol. 9, no. 1, pp. 501-505, 2008.

[41] G. Lippmann, *Inn. Chim. Phys.,* vol. 5, p. 56, 1875.

[42] J. Lee, H. Moon, J. Fowler, T. Schoellhammer, and C.-J. Kim, "Electrowetting and electrowetting-on-dielectric for microscale liquid handling," *Sensors and Actuators A: Physical,* vol. 95, no. 2, pp. 259-268, 2002.

[43] B. Berge, "Electrocapillarity and wetting of insulator films by water," *Comptes Rendus De L Academie Des Sciences Serie Ii,* vol. 317, no. 2, pp. 157-163, 1993.

[44] M. Khanna, I. Moirangthem, A. Joseph, A. K. Dubey, and A. Mathur, "A micro-controller based approach for digital microfluidic sensors," *Journal of Statistics and Management Systems,* vol. 20, no. 4, pp. 743-751, 2017.

[45] H. Moon, S. K. Cho, R. L. Garrell, and C.-J. C. Kim, "Low voltage electrowetting-on-dielectric," *Journal of applied physics,* vol. 92, no. 7, pp. 4080-4087, 2002.

[46] Y. P. Lai, Fei; Xu, Cong; Fuchs, Harald; Chi, Lifeng, "In Situ Surface-Modification-Induced Superhydrophobic Patterns with Reversible Wettability and Adhesion " *Advanced Materials (Weinheim, Germany),* vol. 25, no. 12, pp. 1682-1686, 2013.

[47] Y. Lai, C. Lin, J. Huang, H. Zhuang, L. Sun, and T. Nguyen, "Markedly controllable adhesion of superhydrophobic spongelike nanostructure TiO2 films," *Langmuir,* vol. 24, no. 8, pp. 3867-3873, 2008.

[48] S. Barthwal, Y. S. Kim, and S.-H. Lim, "Fabrication of amphiphobic surface by using titanium anodization for large-area three-dimensional substrates," *Journal of colloid and interface science,* vol. 400, pp. 123-129, 2013.

[49] X. Yuan, M. Zheng, L. Ma, and W. Shen, "High-speed growth of TiO2 nanotube arrays with gradient pore diameter and ultrathin tube wall under high-field anodization," *Nanotechnology,* vol. 21, no. 40, p. 405302, 2010.

[50] Y. Lai, X. Gao, H. Zhuang, J. Huang, C. Lin, and L. Jiang, "Designing Superhydrophobic Porous Nanostructures with Tunable Water Adhesion," *Advanced Materials,* vol. 21, no. 37, pp. 3799-3803, 2009.

[51] C.-F. Wang *et al.*, "Stable superhydrophobic polybenzoxazine surfaces over a wide pH range," *Langmuir,* vol. 22, no. 20, pp. 8289-8292, 2006.

[52] Z. Guo, F. Zhou, J. Hao, and W. Liu, "Stable biomimetic super-hydrophobic engineering materials," *Journal of the American Chemical Society,* vol. 127, no. 45, pp. 15670-15671, 2005.

[53] G. Wang, S. Liu, S. Wei, Y. Liu, J. Lian, and Q. Jiang, "Robust superhydrophobic surface on Al substrate with durability, corrosion resistance and ice-phobicity," *Scientific reports,* vol. 6, p. 20933, 2016.

[54] Z. Cui, Q. Wang, Y. Xiao, C. Su, and Q. Chen, "The stability of superhydrophobic surfaces tested by high speed current scouring," *Applied Surface Science,* vol. 254, no. 10, pp. 2911-2916, 2008.

[55] C. Extrand and S. I. Moon, "Repellency of the lotus leaf: contact angles, drop retention, and sliding angles," *Langmuir,* vol. 30, no. 29, pp. 8791-8797, 2014.

[56] X. Zhu *et al.*, "Robust superhydrophobic surfaces with mechanical durability and easy repairability," *Journal of Materials Chemistry,* vol. 21, no. 39, pp. 15793-15797, 2011.

[57] T. Maitra, C. Antonini, M. A. der Mauer, C. Stamatopoulos, M. K. Tiwari, and D. Poulikakos, "Hierarchically nanotextured surfaces maintaining superhydrophobicity under severely adverse conditions," *Nanoscale,* vol. 6, no. 15, pp. 8710-8719, 2014.

[58] A. Raman, M. Dubey, I. Gouzman, and E. S. Gawalt, "Formation of self-assembled monolayers of alkylphosphonic acid on the native oxide surface of SS316L," *Langmuir,* vol. 22, no. 15, pp. 6469-6472, 2006.

[59] Z. Chu and S. Seeger, "Superamphiphobic surfaces," *Chemical Society Reviews,* vol. 43, no. 8, pp. 2784-2798, 2014.

[60] B. Bhushan, K. Koch, and Y. C. Jung, "Nanostructures for superhydrophobicity and low adhesion," *Soft Matter,* vol. 4, no. 9, pp. 1799-1804, 2008.

[61] N. Kantor-Uriel, P. Roy, S. Saris, V. Kiran, D. H. Waldeck, and R. Naaman, "Evidence for enhanced electron transfer by multiple contacts between self-assembled organic monolayers and semiconductor nanoparticles," *The Journal of Physical Chemistry C,* vol. 119, no. 28, pp. 15839-15845, 2015.

[62] E. Balaur, J. M. Macak, H. Tsuchiya, and P. Schmuki, "Wetting behaviour of layers of TiO2 nanotubes with different diameters," *Journal of Materials Chemistry,* vol. 15, no. 42, pp. 4488-4491, 2005.

[63] E. Balaur, J. M. Macak, L. Taveira, and P. Schmuki, "Tailoring the wettability of TiO 2 nanotube layers," *Electrochemistry Communications,* vol. 7, no. 10, pp. 1066-1070, 2005.

[64] H. C. H. T. Solutions. (2014, dec 21). *Fouling*. Available: http://www.hcheattransfer.com/fouling1.html

[65] A. M. Gil K. Dhawan Ph.D. P.E., Inc. (2007). *Solutions to Membrane Fouling*. Available: http://www.watertreatmentguide.com/membrane_fouling_solutions.htm

[66] M. Olde Riekerink, J. Terlingen, G. Engbers, and J. Feijen, "Selective etching of semicrystalline polymers: CF4 gas plasma treatment of poly (ethylene)," *Langmuir,* vol. 15, no. 14, pp. 4847-4856, 1999.

[67] N. Shirtcliffe, G. McHale, M. Newton, and C. Perry, "Wetting and wetting transitions on copper-based super-hydrophobic surfaces," *Langmuir,* vol. 21, no. 3, pp. 937-943, 2005.

[68] M. Khorasani, H. Mirzadeh, and Z. Kermani, "Wettability of porous polydimethylsiloxane surface: morphology study," *Applied Surface Science,* vol. 242, no. 3, pp. 339-345, 2005.

[69] L. Zhai, F. Ç. Cebeci, R. E. Cohen, and M. F. Rubner, "Stable superhydrophobic coatings from polyelectrolyte multilayers," *Nano letters,* vol. 4, no. 7, pp. 1349-1353, 2004.

[70] Y. Rahmawan, L. Xu, and S. Yang, "Self-assembly of nanostructures towards transparent, superhydrophobic surfaces," *Journal of Materials Chemistry A,* vol. 1, no. 9, pp. 2955-2969, 2013.

[71] K. Ogawa, M. Soga, Y. Takada, and I. Nakayama, "Development of a transparent and ultrahydrophobic glass plate," *Japanese journal of applied physics,* vol. 32, no. 4B, p. L614, 1993.

[72] G. Davaasuren, C.-V. Ngo, H.-S. Oh, and D.-M. Chun, "Geometric study of transparent superhydrophobic surfaces of molded and grid patterned polydimethylsiloxane (PDMS)," *Applied Surface Science,* vol. 314, pp. 530-536, 2014.

[73] R. G. Karunakaran, C.-H. Lu, Z. Zhang, and S. Yang, "Highly transparent superhydrophobic surfaces from the coassembly of nanoparticles ($\leqslant$ 100 nm)," *Langmuir,* vol. 27, no. 8, pp. 4594-4602, 2011.

[74] N. Yokoi, K. Manabe, M. Tenjimbayashi, and S. Shiratori, "Optically transparent superhydrophobic surfaces with enhanced mechanical abrasion resistance enabled by mesh structure," *ACS applied materials & interfaces,* vol. 7, no. 8, pp. 4809-4816, 2015.

[75] A. Nakajima, K. Hashimoto, T. Watanabe, K. Takai, G. Yamauchi, and A. Fujishima, "Transparent superhydrophobic thin films with self-cleaning properties," *Langmuir,* vol. 16, no. 17, pp. 7044-7047, 2000.

[76] M. Miyauchi and H. Tokudome, "Super-hydrophilic and transparent thin films of TiO 2 nanotube arrays by a hydrothermal reaction," *Journal of Materials Chemistry,* vol. 17, no. 20, pp. 2095-2100, 2007.

[77] S. Hoshian, V. Jokinen, and S. Franssila, "Robust hybrid elastomer/metal-oxide superhydrophobic surfaces," *Soft matter,* vol. 12, no. 31, pp. 6526-6535, 2016.

[78] X. Zhang, Y. Guo, Z. Zhang, and P. Zhang, "Self-cleaning superhydrophobic surface based on titanium dioxide nanowires combined with polydimethylsiloxane," *Applied Surface Science,* vol. 284, pp. 319-323, 2013.

[79] J. N. Lee, C. Park, and G. M. Whitesides, "Solvent compatibility of poly (dimethylsiloxane)-based microfluidic devices," *Analytical chemistry,* vol. 75, no. 23, pp. 6544-6554, 2003.